

DYNAMICAL OUTCOMES OF PLANET–PLANET SCATTERING

SOURAV CHATTERJEE,¹ ERIC B. FORD,^{2,3,4} SOKO MATSUMURA,¹ AND FREDERIC A. RASIO¹*Draft version September 16, 2018*

ABSTRACT

Observations in the past decade have revealed extrasolar planets with a wide range of orbital semi-major axes and eccentricities. Based on the present understanding of planet formation via core accretion and oligarchic growth, we expect that giant planets often form in closely packed configurations. While the protoplanets are embedded in a protoplanetary gas disk, dissipation can prevent eccentricity growth and suppress instabilities from becoming manifest. However, once the disk dissipates, eccentricities can grow rapidly, leading to close encounters between planets. Strong planet–planet gravitational scattering could produce both high eccentricities and, after tidal circularization, very short-period planets, as observed in the exoplanet population. We present new results for this scenario based on extensive dynamical integrations of systems containing three giant planets, both with and without residual gas disks. We assign the initial planetary masses and orbits in a realistic manner following the core accretion model of planet formation. We show that, with realistic initial conditions, planet–planet scattering can reproduce quite well the observed eccentricity distribution. Our results also make testable predictions for the orbital *inclinations* of short-period giant planets formed via strong planet scattering followed by tidal circularization.

Subject headings: methods: n-body simulations, methods: numerical, (stars:) planetary systems, (stars:) planetary systems: protoplanetary disks, planetary systems: formation — celestial mechanics

1. INTRODUCTION

The study of extrasolar planets and their properties has become a very exciting area of research over the past decade. Since the detection of the planet 51 Peg b, more than 200 new planets (Butler et al. 2006, see also <http://exoplanet.eu/>) have been detected and the large sky surveys planned for the near future can potentially detect many more. These detections have raised many questions about the formation and dynamical evolution of planetary systems. The extrasolar planet population covers a much greater portion of the semimajor axis and eccentricity plane than was expected based on the planets in our solar system (Lissauer 1995, Fig. 1). The presence of many giant planets in highly eccentric orbits or in very short-period orbits (the “hot Jupiters”) is particularly puzzling.

Different scenarios have been proposed to explain the high eccentricities. The presence of a distant companion in a highly inclined orbit can increase the eccentricities of the planets around a star through Kozai oscillations (Mazeh et al. 1997; Holman et al. 1997). However, this alone cannot explain the observed eccentricity distribution (Takeda & Rasio 2005). Interaction with the protoplanetary gas disk could either excite or damp the eccentricities depending on the properties of the disk and the orbits. However, the combined effects typically result in eccentricity damping (Artymowicz 1992; Papaloizou & Terquem 2001; Goldreich & Sari 2003; Ogilvie & Lubow 2003). Migration of two planets and

trapping in a mean-motion resonance (MMR) can also pump up the eccentricities efficiently, but this mechanism requires strong damping at the end or termination of migration right after trapping in resonance (Lee & Peale 2002) or else it leads to planet scattering (Sándor & Kley 2006). Zakamska & Tremaine (2004) proposed inward propagation of eccentricity after the outer planets are excited to high eccentricities following a close encounter with a passing star. Using typical values for such interactions with field stars in the solar neighborhood, however, they do not get very high eccentricities. Papaloizou & Terquem (2001); Terquem & Papaloizou (2002); Black (1997) propose a very different formation scenario for planets from protostellar collapse in which both hot Jupiters and eccentric planets at higher semimajor axes are formed naturally; this scenario, however, cannot form sub-Jupiter-mass planets.

In this paper, we explore another promising way to create high eccentricities: strong gravitational scattering between planets in a multi-planet system undergoing dynamical instability (Rasio & Ford 1996; Weidenschilling & Marzari 1996; Lin & Ida 1997). According to the model of oligarchic growth, planetesimals form in a nearly maximally packed configuration in the protoplanetary disk, followed by gas accretion (Goldreich et al. 2004; Ida & Lin 2004b; Kokubo & Ida 2002). Once the disk dissipates, mutual planetary perturbations (“viscous stirring”) of the planetesimals will lead to eccentricity growth, orbit crossing, and eventually close encounters between the big bodies in the disk (Ford & Chiang 2007; Levison & Morbidelli 2007). While planetary systems with more than two planets can not be provably stable, they can remain stable for very long timescales depending on their initial separations (Chambers et al. 1996; Marzari & Weidenschilling 2002). A sufficiently massive disk can prevent interacting

¹ Department of Physics and Astronomy, Northwestern University, Evanston, IL 60208

² Harvard-Smithsonian Center for Astrophysics, Mail Stop 51, 60 Garden Street, Cambridge, MA 02138

³ Department of Astronomy, University of Florida, 211 Bryant Space Science Center, P.O. Box 112055, Gainesville, FL, 32611

⁴ Hubble Fellow

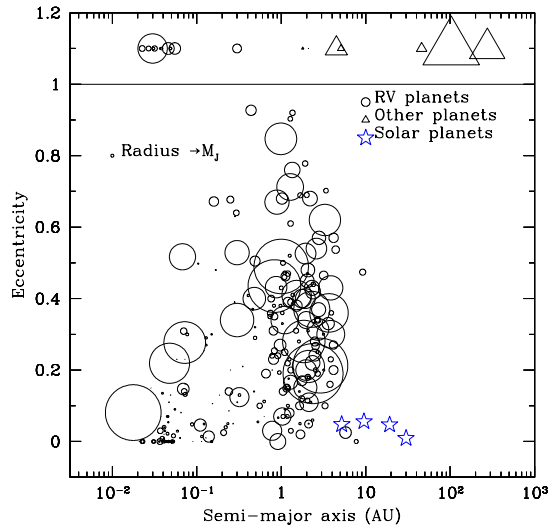


FIG. 1.— Semi-major axis vs eccentricity for the detected planets. The sizes of the points are proportional to the minimum masses ($m \sin i$) of the corresponding planets. The size of a Jupiter mass planet is shown at the left top corner for reference. The stars represent the four giant planets in our solar system (for these the sizes do not indicate their mass). The open circles show the planets detected by radial velocity surveys. The triangles show planets detected by micro-lensing or direct imaging. Planets with poorly constrained eccentricities are plotted above $e = 1$. A horizontal line is drawn at $e = 1$ to guide the eye. Note the logarithmic scale for the semi-major axis.

planets from acquiring large eccentricities and developing crossing orbits. However, once the gas disk is sufficiently dissipated, and the planetesimal disk depleted, the eccentricities of the planets can grow to high values, possibly leading to strong planet–planet scattering and a phase of chaotic evolution that dramatically alters the orbital structure of the system (Lin & Ida 1997; Ford & Chiang 2007; Levison & Morbidelli 2007).

The detection of close-in planets with orbital periods as short as ~ 1 d, the so-called “hot Jupiters” (and, more recently, hot Neptunes and super-Earths), was another major surprise. Giant planets are most likely to form at much larger separations, beyond the ice line of the star where there can be enhanced dust production (Kokubo & Ida 2002; Ida & Lin 2004b). It is widely believed that the giant planets form beyond the ice line and then migrate inwards to form the hot Jupiters we observe today. Different stopping mechanisms of inward migration have been proposed to explain the hot Jupiters, but it is unclear why they pile up at just a few solar radii around the star, rather than continue migrating and eventually accrete onto the star.

Strong gravitational scattering between planets in a multi-planet system may provide another way to create these close-in planets (Rasio & Ford 1996). A few of the planets scattered into very highly eccentric orbits could have sufficiently small periastron distances that tidal circularization takes place, giving rise to the hot Jupiters. The currently observed edge in the mass-period diagram is very nearly at the ideal circularization radius (twice the Roche limit), providing support for this model (Ford & Rasio 2006). Faber et al. (2005) finds that these violent passages might not destroy the planets, even if

mass loss occurs.

Previous studies have investigated gas free systems with two planets around a central star extensively (Rasio & Ford 1996; Ford et al. 2001, 2003; Ford & Rasio 2007) and have also begun to investigate the dynamics of two planets in the presence of a gas disk by using simplified prescriptions for dissipative effects (Moorhead & Adams 2005). The observed eccentricity distribution is not easily reproduced by two equal-mass planets (Ford et al. 2001). However, strong scattering of two *unequal-mass* planets could explain the observed eccentricities of most observed exoplanets (Ford et al. 2003; Ford & Rasio 2007).

A system with three planets is qualitatively different than one with two planets. In two-planet systems, there is a sharp boundary between initial conditions that are provably Hill stable and initial conditions that quickly lead to a close encounter (Gladman 1993). Moreover, for two Jupiter-mass planets in close to circular orbits, this boundary lies where the ratio of orbital periods is less than 2:1. If these planets formed further apart, then a slow and smooth migration could lead to systems becoming trapped in a 2:1 MMR before triggering an instability (Lee & Peale 2002; but see Sándor & Kley 2006). These stability properties are in sharp contrast to those of systems with three or more planets, for which there is no sharp stability boundary. These systems can become unstable even for much wider initial spacings and the timescale to the first close encounter can be very long (Chambers et al. 1996). Even if all pairs of adjacent planets in the system are stable according to the two-planet criterion, the combined system can evolve in a chaotic (but apparently bounded) manner for an arbitrarily long time period before instability sets in. This timescale to instability can easily exceed other timescales of interest here such as those for the formation of giant planets, orbital migration, or dispersal of the gas disk. Therefore, the stability properties of three-planet systems can be studied with long-term orbital integrations without the need to implement any additional physics.

A pioneering study of the stability and final orbital properties of three-planet systems was performed by Marzari & Weidenschilling (2002, hereafter MW02). They explored the basic nature of instabilities arising in systems with three giant planets around a central solar-like star, and they determined the final orbital properties after one planet is ejected. This study used highly idealized initial conditions with three equal-mass planets or with one arbitrary mass distribution (middle planet twice as massive as the other two). It was also computationally limited to a rather small ensemble of systems.

Our two main goals in this new work were to extend the work of MW02 by using more realistic initial conditions (see §2) and to perform a much more extensive numerical survey in order to fully characterize the statistical properties of outcomes for unstable three-planet systems. Given the chaotic nature of the dynamics, one needs to integrate many independent systems to characterize the statistical properties of the final planetary orbits (see a detailed analysis for the dependence of various statistics on the sample size in Appendix A; see also Adams & Laughlin 2003). Each system has to be integrated for a long time, so that it reaches the orbit-crossing unstable phase and later evolves into a new, sta-

ble configuration. Given the rapid increase in computing power, we are now able to perform significantly more and longer integrations to obtain much better statistical results than was possible just a few years ago.

In addition, we also present the results of new simulations for systems of three giant planets still embedded in a residual gas disk. Here our goal is different: we focus on the transition from gas-dominated to gas-free systems, in the hope of better justifying the (gas-free) initial conditions adopted in the first part of our work. However, implementing the physics of planet-disk interactions implies a considerably higher computational cost, preventing us from doing a complete statistical study of outcomes at this point.

2. GAS-FREE SYSTEMS WITH THREE GIANT PLANETS

In this section we consider systems with three unequal-mass giant planets orbiting a central star of mass $1 M_\odot$ at distances of several AU. The planets interact with each other through gravity and physical collisions only. We first present our assumptions and initial conditions, with particular emphasis on realistic mass distributions for the planets, and then we describe our numerical results and their implications.

2.1. Initial Orbits

For all systems the initial semimajor axis of the closest planet is always set at $a_1 = 3 \text{ AU}$. The other two planets are placed using the spacing law introduced by MW02,

$$a_{i+1} = a_i + K R_{H,i}, \quad (1)$$

where $R_{H,i}$ is the Hill radius of the i^{th} planet and we set $K = 4.4$ for all runs in this section. These choices are somewhat arbitrary, but are guided by the following considerations. For a solar-mass central star, the ice line is around 3 AU (Kokubo & Ida 2002) and it is difficult to form giant planets closer to the star (see e.g., Kokubo & Ida 2002). Although inward type II migration (see e.g., Goldreich & Tremaine 1980) can bring the giant planets closer to the star, we avoid putting the planets initially very close to the star since very small initial semi-major axis will lead to predominantly collisional outcomes. Furthermore, we would like to minimize the computing time, which leads us to consider closely spaced systems, while avoiding MMRs.

Since our simulations in this section do not include the effects of gas, they are not intended to model the early phases of planet formation. Instead, at $t = 0$, we begin integrating fully formed planetary systems with a disk sufficiently depleted that the planets are free to interact with each other without significant dissipation from the disk. In §2.4, we show that the time until instability within a particular set of initial conditions does not affect the statistical properties of final outcomes. Indeed, we expect that the chaotic dynamics, both *before* and *after* the first close encounter, results in the distribution of final outcomes being independent of the instability timescale. This justifies our choice of a very compact initial configuration with short instability timescale ($\sim 10^4 \text{ yr}$), which minimizes the computational cost. See MW02 and Appendix B for further discussion of the dependence of the instability timescale on K .

Initial eccentricities are drawn from a uniform distribution between 0–0.1, and orbital inclinations are drawn

from a uniform distribution between 0° – 10° (with respect to the initial orbital plane of the innermost planet). To make sure that we could discern any inclination-dependent effects we used a slightly broader range of inclinations than seen in our solar system. However, in §2.6, we show numerically that the choice of initial inclinations does not affect the distribution of final inclinations significantly. All initial phase angles are assigned random values between 0° – 360° .

2.2. Planetary Mass Distributions

Our current understanding of planet formation remains full of uncertainties and no single prescription can claim to predict a correct planet mass distribution. For this reason, we consider three different prescriptions to construct plausible initial mass distributions for Jupiter-like planets. In all cases we adopt the standard core-accretion paradigm and we closely follow the simple planet formation model described in Kokubo & Ida (2002, hereafter KI02). Planet masses depend on the distance of the planet from the central star through the gas surface density profile of the protoplanetary disk.

2.2.1. Mass Distribution 1

In this prescription, we first assign the planetary core masses M_{core} assuming a uniform distribution between 1 – $10 M_\oplus$. We assume that the cores accrete all gas within 4 Hill radii (KI02) to reach a total mass M at a semimajor axis a given by

$$M = 2\pi a \Delta \Sigma_{\text{gas}} + M_{\text{core}}, \quad (2)$$

where $\Delta = 8r_H$ is the feeding zone of the planet core and r_H is the Hill radius of the planet core, given by

$$r_H = \left(\frac{1}{3} \frac{M_{\text{core}}}{M_\star} \right)^{1/3} a. \quad (3)$$

Here M_\star is the mass of the central star and a is the orbital radius of the core (assumed to be on a circular orbit). The gas surface density in the disk is given by

$$\Sigma_{\text{gas}} = f_g \Sigma_1 \left(\frac{a}{1 \text{ AU}} \right)^{-\frac{3}{2}} \text{ g cm}^{-2}, \quad (4)$$

where the coefficient $f_g = 240$ is the assumed gas-to-dust ratio (taken from KI02), Σ_1 is the surface density at 1 AU, and the exponent comes from the minimum-mass disk model. We use $\Sigma_1 = 10$ in this case, which is a little higher than the minimum-mass Solar nebula value of 7. The choice of Σ_1 is somewhat arbitrary and motivated to produce roughly Jupiter-mass planets. The initial masses of the planets obtained with this procedure are between about $0.4 M_J$ and $1.2 M_J$.

For this mass distribution we performed a set of 1000 independent dynamical runs.

2.2.2. Mass Distribution 2

This is a slight refinement on the previous case in which we adopt an alternative prescription for accretion that takes explicitly into account the growing mass of the initial planetary core. The initial core masses are chosen as in §2.2.1 but the final mass of each planet is now determined using the following equations. Assuming that

an infinitesimal mass dm accreted by a planet of mass m decreases the disk density by $d\Sigma$, we can write

$$dm = -2\pi a n_H r_H d\Sigma, \quad (5)$$

where n_H is the number of Hill radii over which the mass is accreted. The final mass M of a planet at a distance a from the star, starting with a core mass M_{core} can be obtained by integrating Eq. 5 as follows,

$$\int_{M_{\text{core}}}^M m^{-1/3} dm = -2\pi n_H a^2 \frac{1}{3M_\star^{1/3}} \int_{\Sigma_i}^0 d\Sigma, \quad (6)$$

where Σ_i is the initial disk surface mass density. Solving Eq. 6 and replacing Σ_i from Eq. 4 we find

$$M = \left(\frac{4\pi n_H a^2}{M_\star^{1/3} 3^{4/3}} f_g \Sigma_1 \left(\frac{a}{1\text{AU}} \right)^{-3/2} + m_c^{2/3} \right)^{3/2}. \quad (7)$$

Here we use $n_H = 8$, i.e., we assume that the core accretes all mass within 4 Hill radii on either side. We use the same values for f_g and Σ_1 from §2.2.1.

For this mass distribution we have integrated a smaller set of 224 systems.

2.2.3. Mass Distribution 3

We expect that the final distributions of different orbital properties may vary significantly with different initial mass distribution. To further test this mass dependence, we created a third set of systems with a broader planet mass distribution. Here we assign planetary masses exactly as in §2.2.1, but the initial core masses are chosen differently. We sample M_{core} from a distribution of masses between $1\text{--}100 M_\oplus$ uniform in $M_{\text{core}}^{1/5}$, while assuming again that these cores accrete all gas within 8 Hill radii. The exponent in the core mass distribution and the surface density at 1 AU, $\Sigma_1 = 15$, are chosen somewhat arbitrarily with the goal to obtain an initial mass distribution that peaks around a Jupiter mass but with a tail extending up to several Jupiter masses. The choices above produce initial masses spanning about an order of magnitude, in the range $0.4 M_J\text{--}4 M_J$. Moreover, the distribution for higher-mass planets resembles the mass distribution of observed exoplanets (see §2.8).

For this mass distribution we have integrated a set of 500 systems.

2.3. Numerical Integrations

We integrate each system for 10^7 yr, which is 2×10^6 times the initial period of the closest planet ($T_{1,i}$), and typically much longer than the timescale for the onset of instability. We use the hybrid integrator of MERCURY6.2 (Chambers 1999) and integrate the orbits symplectically while there is no close encounter, with a time-step of 10 days, but switching to a Bulirsch-Stoer (BS) integration as soon as two planets have a close approach (defined to be closer than 3 Hill radii). Runs with poor energy conservation ($|\Delta E/E| \geq 0.001$) with the hybrid integrator are repeated using the BS integrator throughout with the same $|\Delta E/E|$ tolerance. This happens in $\sim 30\%$ of all runs, but our conclusions are not affected even if we reject these systems. We find that, in all systems, at least one planet is eventually ejected. Note that, for three-planet systems, following an ejection the remaining two

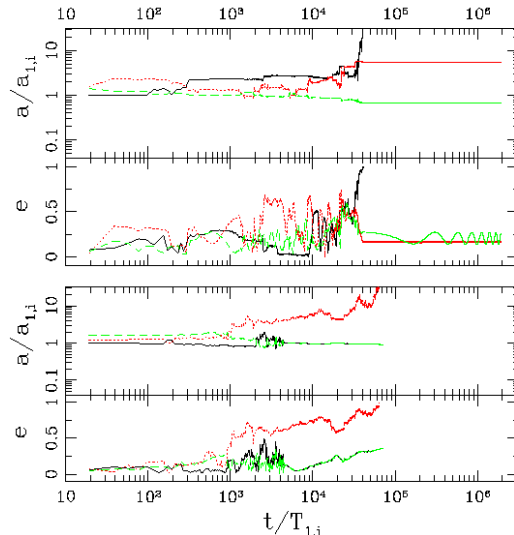


FIG. 2.— Time evolution of semi-major axes and eccentricities for two randomly chosen typical simulations. The solid (black), dotted (red), and dashed (green) lines show the orbital elements for the initially closest (a_1, e_1), middle (a_2, e_2), and furthest (a_3, e_3) planets. The top pair of panels show a realization where the first planet is ejected at $\sim 4.1 \times 10^4 T_{1,i}$, and the integration concludes with two planets in provably stable orbits. The semi-major axes for both P_2 and P_3 remain constant and the eccentricities oscillate stably on a secular timescale. The bottom pair shows another realization where P_3 collides with P_1 at $\sim 4.2 \times 10^3 T_{1,i}$; e_2 keeps increasing until, a little before $10^5 T_{1,i}$, P_2 gets ejected, leaving a single planet in the system. Since a single orbit is always stable we stop the integration following this ejection. Numbers in the subscript represent the positional sequence of the planets starting from the star and letters “i” and “f” mean initial and final values, respectively, in all plots.

planets may or may not be dynamically unstable. Therefore, we do not stop the integration following an ejection. Instead, we continue all integrations for two planets until a fixed stopping time of 10^7 yr. For systems with two remaining planets we check for Hill stability using the known semi-analytic criterion (Gladman 1993). In our simulations about 9% of systems were not provably Hill stable at the integration stopping time. We discard those from our analysis. When a single planet remains (following a second ejection or when a collision took place), the integration is of course stopped immediately.

For systems with two remaining dynamically stable planets the orbits can still evolve on a secular timescale (typically $\sim 10^5\text{--}10^6$ yr for our simulated systems) much larger than the dynamical instability timescale (Adams & Laughlin 2006a; see also Murray & Dermott 2000, Ch 7). We study these systems with two remaining stable planets by integrating the secular perturbation equations for a further 10^9 yr with the analytical formalism developed in Ford et al. (2000). Note that the more standard formulation for Solar system dynamics (Murray & Dermott 2000) is not appropriate for these planetary systems because a significant fraction present very high eccentricities and inclinations. We find that for most of our simulated systems our chosen integration stopping time effectively sampled the full parameter space (see detailed discussion in §2.9).

We treat collisions between planets in the following simple way (“sticky-sphere” approximation). A collision

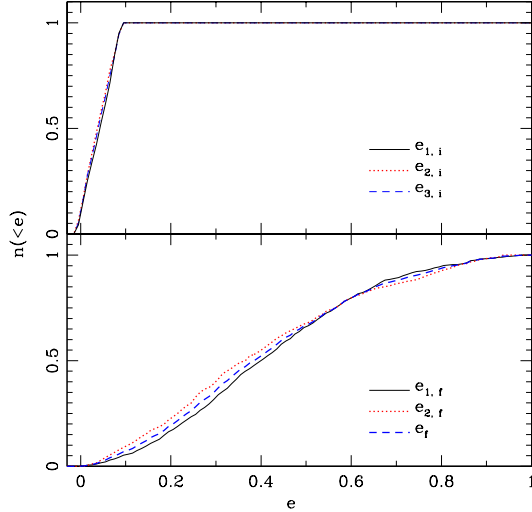


FIG. 3.— Cumulative distributions showing initial and final eccentricities of the planets. Top and bottom panels show the initial and final cumulative eccentricity distributions, respectively. In the top panel solid (black), dotted (red) and dashed (blue) lines represent the closest, middle, and furthest planets, respectively. They are on top of each other because the initial eccentricity distribution is the same for all of the planets. In the bottom panel solid (black) and dotted (red) lines represent the final inner and outer planets, respectively. The dashed (blue) line shows all remaining planets in final stable orbits.

is assumed to happen when the distance between two planets becomes less than the sum of their physical radii. We assume Jupiter’s density (1.33 g cm^{-3}) for all planets when determining the radius from the mass. After a collision the two planets are replaced by a single one conserving mass and linear momentum. Because we account for collisions, our results are not strictly scale free. However, we find that collisions are relatively rare for our choice of initial conditions, so we still present all results with lengths scaled to $a_{1,i}$ and times scaled to $T_{1,i}$.

Since Mass Distribution 1 corresponds to our largest set of runs, we first show our results from this set in detail in the following subsections (§2.4 – §2.7). Results for the other two sets are summarized in §2.8.

2.4. Overview of Results

In Fig. 2 we show a couple of randomly selected, representative examples of the dynamical evolution of these systems, showing both chaotic phases and stable final configurations. Note the order-of-magnitude difference in timescale to first orbit crossing, illustrating the broad range of instability timescales (see also the discussion in Appendix B). We find that strong scattering between planets increases the eccentricities very efficiently (Fig. 3). The median of the eccentricity distribution for the final inner planets is 0.4. The median eccentricity for the final outer planets is 0.37, that for all simulated planets in their final stable orbits, is ~ 0.38 .

We compare our results with the observed eccentricity distribution of detected exoplanets in Fig. 4. For a more meaningful comparison we restrict our attention to observed planets with masses greater than $0.4 M_J$, similar to the lower mass cut-off in our simulated systems. We also place an upper limit on the semimajor axis at 10 AU

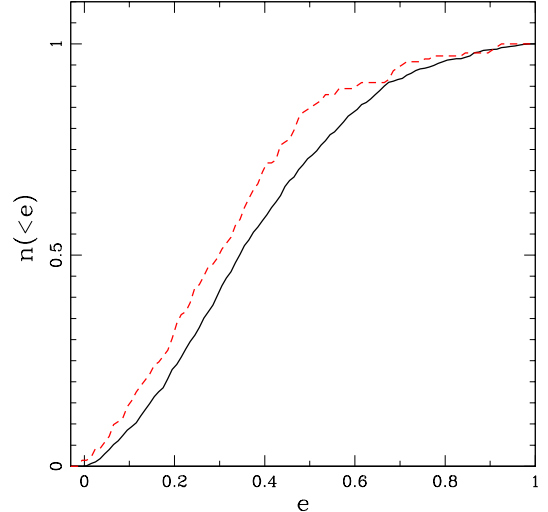


FIG. 4.— Comparison between the simulated and observed exoplanet populations. The solid (black) line shows the cumulative distribution of the eccentricities of the remaining planets in their final stable orbits. The dashed (red) line is that for the observed population. For this comparison we employ a lower mass cut-off of $0.4 M_J$ on the observed population addressing the fact that we do not have lower mass planets in our simulations. We also consider only the simulated planets that are finally within 10 AU from the star to address the fact that in the observed population we do not have planets further out. We also employ a lower semi-major axis cut-off of $0.1 a_{1,i}$ on the observed population.

for the simulated final planet population to address the observational selection effects against discovering planets with large orbital periods. Similarly, since planets close to the central star can be affected by additional physics beyond the scope of this study (e.g., tides, general relativistic effects; see Adams & Laughlin 2006b) we also omit observed close-in planets with semimajor axes below $0.1 a_{1,i}$.

As seen in Fig. 3 and Fig. 4, our simulations slightly overestimate the eccentricities of the planetary orbits. However, the slopes of the cumulative eccentricity distributions at higher eccentricity values are similar. In a realistic planetary system, there might be damping effects from lingering gas, dust or planetesimals in a protoplanetary disk. While our simplified models already come close to matching the eccentricity distribution of observed planets, including damping may further improve this agreement. To be more quantitative, we perform a Kolmogorov-Smirnov (KS) test and find that we cannot rule out the null hypothesis (that the two populations are drawn from the same distribution) at the 85% level (Table 1). In §2.8, we will show that a broader initial distribution of planet masses results in an even better match to the observed eccentricity distribution.

The top and bottom panels in Fig. 5 show the cumulative distributions of the initial vs final semi-major axes for the planets. The planet that is closest to the star initially may not remain closest at the end of the dynamical evolution. In fact, all three planets, independent of their initial positions, have roughly equal probability of becoming the innermost planet in the final stable configuration when the planet masses are not very different. In 20% of the final stable systems, we find a

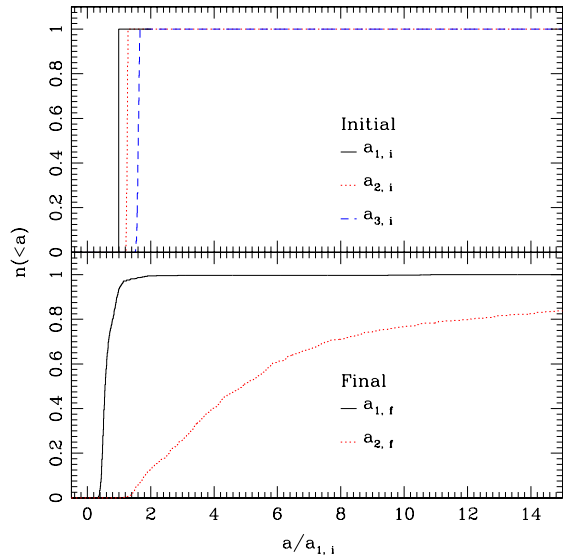


FIG. 5.— Cumulative frequency plots of semi-major axes of the initial (top panel) and final (bottom panel) planets. Vertical solid (black), dotted (red) and dashed (blue) lines show the initial values in the top panel. These are vertical lines because the initial semi-major axes of the closest, middle and outer planets do not have a spread. Solid (black) and dotted (red) curves in the bottom panel show the final inner and outer planets’ semi-major axes, respectively.

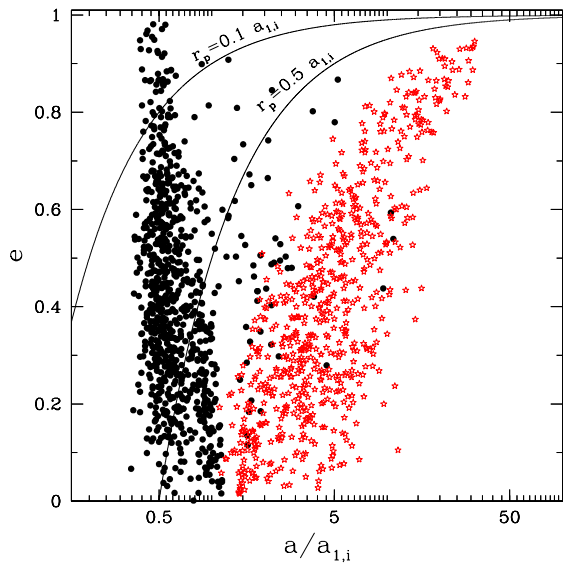


FIG. 6.— Final semi-major axis versus eccentricity plot. All lengths are scaled by the initial closest planet semi-major axis (here $a_{1,i} = 3.0\text{AU}$). Black solid circles and red open stars represent the final inner and outer planets, respectively. Solid lines show different constant periastron lines with values 0.1 and 0.5. Note the high eccentricities and the close approaches towards the central star. The empty wedge shaped region in the a - e plane at high eccentricities is due to the requirement for orbital stability.

single planet around the central star, two planets having been lost from the system either through some combination of collisions and dynamical ejection. The other systems have two giant planets remaining in stable orbits. We find that the planets in the outer orbits show a tendency for higher eccentricities correlating with larger semi-major axes (Fig. 6). We now know that many of

TABLE 1
COMPARISON OF ECCENTRICITY
DISTRIBUTIONS

	D	P
Mass distribution 1	0.113	0.15
Mass distribution 2	0.171	0.01
Mass distribution 3	0.087	0.32

^a For each mass distribution, we compare the final eccentricity distribution of the simulated population with the observed exoplanet population (Figs. 4, 18). Using the `kstwo` function in `Numerical Recipes`, we calculate the two-sample Kolmogorov-Smirnov statistic, D , and the corresponding probability, P . In each case, the high value of P indicates that we can not reject the null hypothesis that both samples were drawn from the same population.

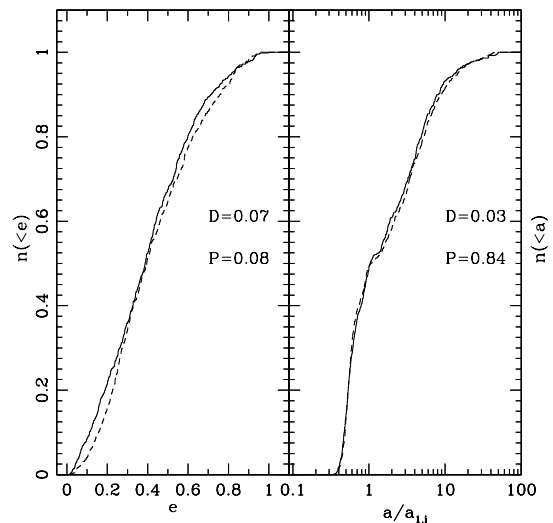


FIG. 7.— Left panel: cumulative frequency plots for the final eccentricities of the two subgroups, *Group 1* (solid line) and *Group 2* (dashed line). Right panel: cumulative frequency plots for the final semi-major axes of the two subgroups, *Group 1* (solid line) and *Group 2* (dashed line). KS statistics results, D and P are also quoted for each of the above. D and P are as defined in Table 1.

the current observed exoplanets may have other planets in distant orbits (Wright et al. 2007). From our results we expect that planets scattered into very distant bound orbits will have higher eccentricities. Long-term radial velocity monitoring should be able to test this prediction.

Next, we investigate to what extent the final orbital properties depend on the instability timescale (equivalently, on how closely packed the initial configuration was). For each system we integrated in §2.2.1, we noted the first time when the semi-major axis of any one of the planets in the system changed by at least 10%. We use this as a measure of the dynamical instability growth timescale. Then, we divide the set into two subgroups, based on whether this growth time was below (*Group 1*) or above (*Group 2*) its *median* value (so 50% of the in-

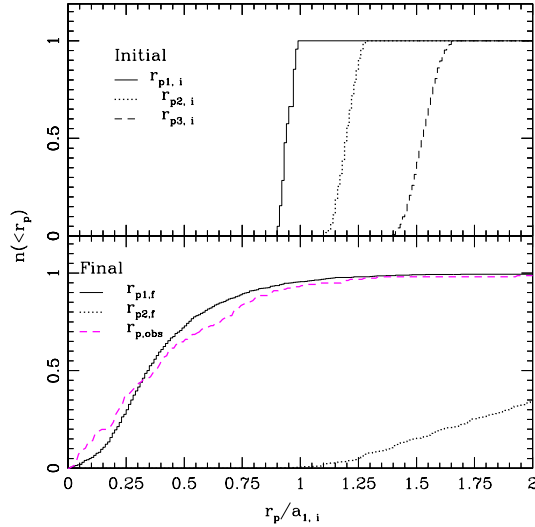


FIG. 8.— Cumulative histogram of the pericenter distance of the initial (top panel) and final (bottom panel) planets bound to the star. In the top panel the solid, dotted and dashed lines show the pericenter distributions of the initial closest, middle and the furthest planets, respectively. In the bottom panel the solid and dotted lines show the same for the final stable inner and the outer planets with their semi-major axes less than 10 AU. The dashed magenta line shows the pericenter distribution of the observed exoplanet population for comparison purposes.

tegrated systems are in each group). Fig. 7 compares the final eccentricity and semi-major axis distributions between the two groups. We find that the distributions are indistinguishable, demonstrating that the final (observable) orbital properties are not sensitive to when exactly a particular system became dynamically unstable, as long as the dynamics was sufficiently active (ensuring that close encounters occur) and avoiding initial conditions so closely packed that physical collisions would become dominant. This result is hardly surprising since we expect the chaotic evolution to efficiently erase any memory of the initial orbital parameters. Our results can therefore be taken as representative of the dynamical outcome for analogous systems with an even larger initial spacing between planets (but avoiding mean motion resonances; see Appendix B). In practice, performing a large number of numerical integrations for these more widely spaced initial configurations would be prohibitively expensive (see Appendix B).

2.5. Hot Jupiters from Planet–Planet Scattering

We find that a significant fraction of systems emerge with planets in orbits having very small periastron distances. Fig. 6 shows the final positions of the planets that are still bound to the central star in the $a - e$ plane. The solid lines represent different constant pericenter distances. Note that the planets show weak correlations between the eccentricity and the semi-major axis. For the inner planets, a lower semi-major axis tends to imply higher eccentricity, while the outer planets show an opposite trend. The final inner and outer planets form two clearly separated clusters of points in the $a - e$ plane due to stability considerations.

Fig. 8 shows the cumulative distribution of the periastron distances of the final bound planets around

the star. For the sake of comparison, we also show the pericenter distribution of all observed exoplanets in Fig. 8. We see that 10% of the systems harbor planets with periastron distances $\leq 0.05a_{1,i}$, whereas, a few ($\sim 2\%$) harbor planets with periastron distances $\leq 0.01a_{1,i}$. Since we do not include tidal effects, we cannot compare this quantitatively with the observed population. However, this is consistent with the $\sim 5\%$ of observed planets with semi-major axes within 0.03 AU. If the initial semi-major axes are sufficiently small tidal forces could then become important and a planet on a highly eccentric orbit could be circularized to produce a hot Jupiter (Ford & Rasio 2006; Faber et al. 2005; Rasio & Ford 1996; Weidenschilling & Marzari 1996; Marzari & Weidenschilling 2002). However, recall that systems with much smaller values of $a_{1,i}$ would also lead to more physical collisions than in our simulations. Moreover, a full numerical study of this scenario should include tidal dissipation as part of the dynamical integrations, and possibly also include additional physics such as GR effects, etc. (Nagasawa et al. 2008).

2.6. Planets on High-inclination Orbits

Since the star and planets get their angular momenta from the same source, planetary orbits are generally expected to form in a coplanar disk perpendicular to the stellar spin axis. In Fig. 9, we compare the distributions of the final inclination angles. Here each angle reported is the absolute value of the orbital inclination measured with respect to the initial invariable plane, defined as the plane perpendicular to the initial total angular momentum vector of the planetary orbits. Note that the direction of the initial total angular momentum can differ from the direction of the total angular momentum of the bound planets at the end of a simulation, since planets are frequently ejected from the system, carrying away angular momentum.

Strong scattering between planets often increases inclinations of the orbits, leading to a higher final RMS value of planet inclinations compared to the initial configuration (Fig. 9, top panel). In general, the inclinations tend to increase for all planets. The middle and bottom panels in Fig. 9 show the initial and final inclinations of the orbits of individual planets, respectively. The inclination of the final inner planet is typically larger than that of the final outer planet (Fig. 9, bottom panel).

Our results show that strong planet–planet scattering can dramatically affect the coplanarity of some planetary systems (Fig. 9, bottom panel). Since the timescale for tidal damping of inclinations is usually much greater than the age of the stars (Winn et al. 2005), significantly increased inclinations could be found in some planetary systems that have gone through strong gravitational scattering phases in their lifetimes. Measuring a poor degree of alignment among the planetary orbits in multiple-planet systems, or between the angular momentum of one planet and the spin axis of its host star, could be used to identify systems that have undergone a particularly tumultuous dynamical history.

If a system were initially assigned to a strictly coplanar configuration, then angular momentum conservation dictates that it would remain coplanar always. However, away from this trivial limit, we expect little correlation between the initial and final inclinations, given the

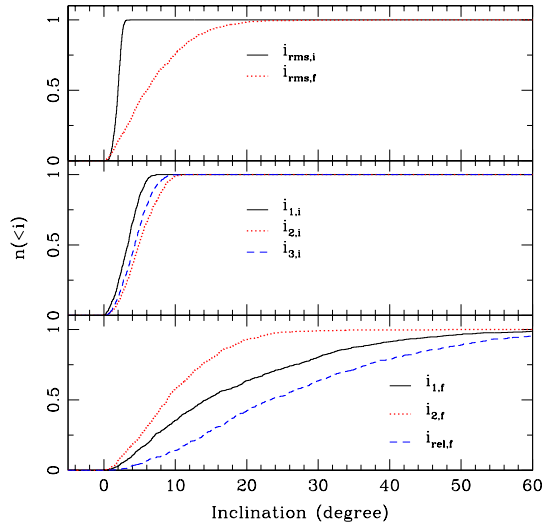


FIG. 9.— Cumulative distribution showing initial and final orbital inclinations of the planets with respect to the initial invariable plane. In the top panel the solid (black) and the dotted (red) lines represent the initial and final RMS inclination distributions of the planet orbits with respect to the initial invariable plane. In the middle panel solid (black), dotted (red) and dashed (blue) lines represent the closest, middle and furthest planets, respectively. The bottom panel shows the final orbital inclination distributions of the remaining planets in the system. The solid (black), and the dotted (red) lines represent the inner and outer planets, respectively. The dashed (blue) line represents the relative angles between the two remaining planetary orbits. Note that the final closer planets, which are the planets more easily observable in a planetary system, statistically have higher inclinations. Note, that the relative inclinations between the planetary orbits are also quite high.

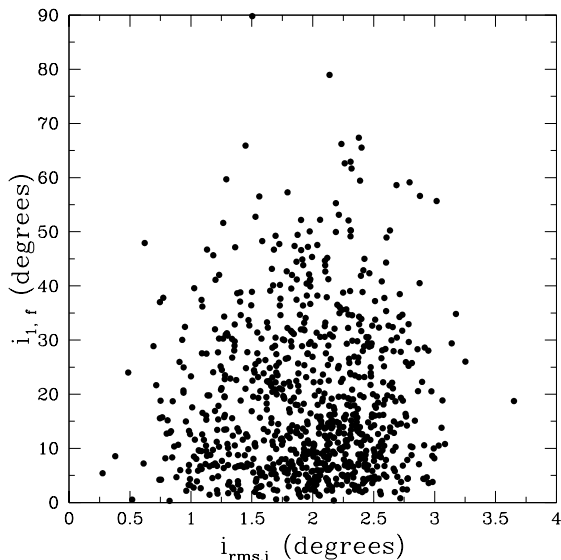


FIG. 10.— Initial RMS inclination vs final inclination of the innermost planet. Note that the final closer planet orbital inclination is largely insensitive to the initial RMS inclination.

chaotic nature of the dynamics. We test this hypothesis here by investigating the correlation between the initial and final inclinations of all planets in our simulations. We find that the final inclination of the inner planet indeed does not depend on the initial RMS inclination

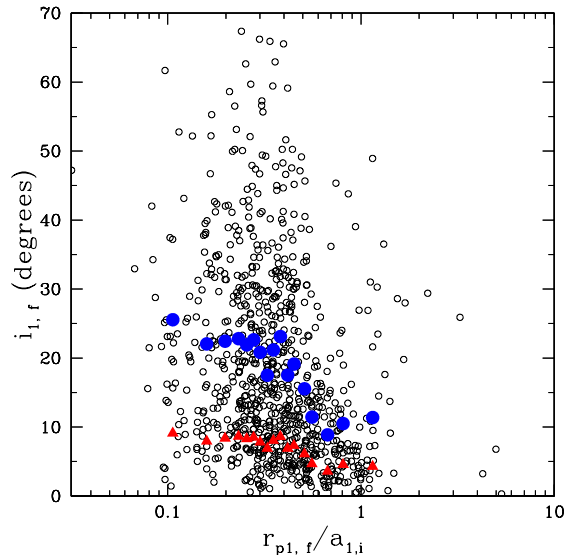


FIG. 11.— Pericenter distance vs inclination of the final inner planets. The open dots show the final positions of the final inner planet in the pericenter-inclination plane. The filled disks (blue) and triangles (red) represent the mean orbital inclination of the inner planet and the final RMS inclinations, respectively. The means are obtained for bins of equal population ($n_{bin} = 50$). We observe a weak anti-correlation between the pericenter and the inclination.

(Fig. 10). We can quantify the amount of correlation between the initial RMS inclination and the final orbital inclination of the final inner planet using the bivariate correlation coefficient. The bivariate correlation coefficient (r_{xy}) for two variables x and y , is given by the following equation,

$$r_{xy} = \frac{\text{Cov}(x, y)}{sd(x)sd(y)}, \quad (8)$$

where $\text{Cov}(x, y)$ is the covariance of x and y , and $sd(x)$ or $sd(y)$ is the standard deviation of x or y . We find that the correlation coefficient between the initial RMS and the final inner planet orbital inclinations is $r_{iRMS,iclose} = 0.05$. The low value of r confirms that the high final inclinations are not merely a reflection of the initial conditions. As long as the planetary system is not strictly coplanar initially, strong planet-planet scattering can increase the orbital inclinations of some systems significantly.

The final inclination of the inner planet, which is the most easily observable, shows a weak anti-correlation with the pericenter distance of its orbit (Fig. 11): lower pericenter orbits tend to have higher inclinations. The correlation coefficient in this case is $r_{rp,iclose} = -0.13$ (Eq. 8).

For our solar system, the angle between the spin axis of the Sun and the invariable plane is $\simeq 6^\circ$. The angle between the stellar rotation axis and the orbital angular momentum of a transiting planet (λ) can be constrained via the Rossiter-McLaughlin effect. Observations have measured $\lambda \sin i$ for five systems (Winn 2006b): $-4.4^\circ \pm 1.4^\circ$ for HD 209458b (Winn et al. 2005), $-1.4^\circ \pm 1.1^\circ$ for HD 189733b (Winn et al. 2006), $11^\circ \pm 15^\circ$ for HD 149026b (Wolf et al. 2007), $30^\circ \pm 21^\circ$ for TrES-1b (Narita et al. 2007a), and, most recently, $62^\circ \pm 25^\circ$ for HD 17156b (Narita et al. 2007b). Our study implies that

planetary systems with a tumultuous dynamical history will sometimes show a large λ . Therefore, we look forward to precise measurements of λ for many planetary systems to determine the fraction of planets among the exoplanet population with a significant inclination. In particular HD 17156b is very interesting in this regard, since the potentially high λ together with the high eccentricity ($e = 0.67$) strongly indicates a dynamical scattering origin for this planet. Measurements of λ would be particularly interesting for the massive short-period planets ($m > M_J$), the very-short period giant planets ($P < 2.5$ d), or the eccentric short period planets, since these planets might have a different formation history than the more common short-period planets with $m \simeq 0.5M_J$ in nearly circular orbits.

2.7. Mean Motion Resonances

The radial-velocity planet population currently includes 20 multi-planet systems and at least 5 of those systems are in MMR (4 appear to be in a 2:1 MMR). MMRs can have strong effects on the dynamical evolution and stability of planetary systems. The 2:1 MMR is particularly interesting given the proximity of the two orbits and the increased possibility for close encounters that could result in strong gravitational scattering between the two planets (Sándor & Kley 2006; Sándor et al. 2007).

It is widely believed that MMRs between two or more planets in a planetary system arise naturally from migration. Convergent migration in a dissipative disk can lead to resonant capture into a stable MMR, particularly the 2:1 MMR (Lee & Peale 2002). Simulations including an empirical dissipative force show that planetary orbits predominantly get trapped in 2:1 MMR (Moorhead & Adams 2005; Nagasawa et al. 2008).

While we regard differential migration as a natural way to trap planets into MMRs, we did explore the possibility of trapping two planets into 2:1 MMR using only the mutual gravitational perturbations and without any damping. We certainly expect this to be more difficult than with damping. Finding even a few systems trapped in MMR without any dissipation would be both surprising and interesting. In a three-planet system it is possible that one planet acts as a source or sink of energy to let the other two planets dynamically evolve into or out of a MMR. If pure dynamical trapping into MMRs were efficient, then this would open up interesting possibilities. For one, it does not require a common disk origin, as is a requirement for the migratory origin of MMRs. Additionally, this mechanism could operate in a planetary system at a much later time after the protoplanetary disk has been dissipated.

To look for possible 2:1 MMR candidates, we isolate systems that have two remaining planets with their final periods close to a 2:1 ratio. Then we calculate the two resonance angles θ_1 and θ_2 over the full time of their dynamical evolution. Here the two resonance angles are given by

$$\theta_{1,2} = \phi_1 - 2\phi_2 + \varpi_{1,2}, \quad (9)$$

where ϕ_1 and ϕ_2 are the mean longitudes of the inner and outer planets and ϖ_1 and ϖ_2 are the longitudes of periastron for the inner and outer planets, respectively. When the planets are not in a MMR, $\theta_{1,2}$ circulate through 2π . When trapped in a MMR, the angles librate around two

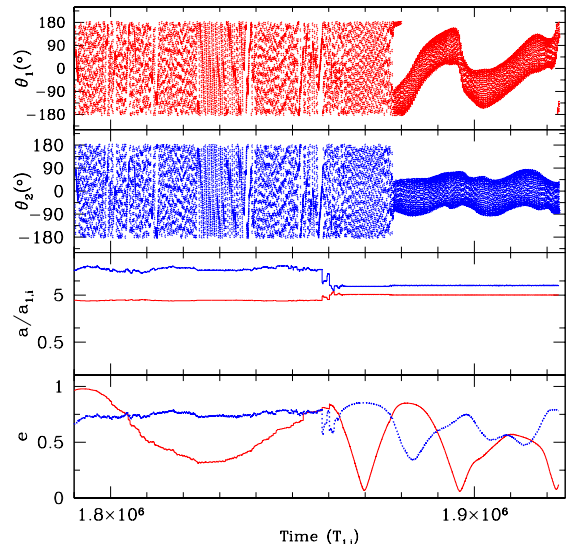


FIG. 12.— Time evolution plots for the two resonance angles θ_1 and θ_2 , the semi-major axes and the eccentricities of the planets. From top to bottom the panels show the time evolutions of θ_1 , θ_2 , semi-major axes and eccentricities, respectively. The time axis is in units of the initial orbital period of the initially closest planet ($T_{1,i}$). For the panels showing semi-major axes and eccentricity, the solid (red) and dotted (blue) lines show the evolutions of the two planets that enter a 2:1 MMR. Note that a little before $1.88 \times 10^6 T_{1,i}$ both θ_1 and θ_2 start librating.

values (Lee 2004). Finally, we check whether the periodic ratio and libration of the resonant angles are long lived or just a transient stage in their dynamical evolution.

We find one system where two planets are clearly caught into a 2:1 MMR (Fig. 12). The top two panels show the time evolution of the resonant arguments θ_1 and θ_2 . The two resonant angles go from the circulating phase to the librating phase at around $1.88 \times 10^6 T_{1,i}$. The two bottom panels show the evolution of the semi-major axes and the eccentricities of the two planets in MMR. Note that the semi-major axes are nearly constant and the eccentricities oscillate stably. Since there is no damping in the system, the somewhat large libration amplitude of the resonant angles is to be expected. In principle, the presence of even a little damping (due to some residual gas or dust in the disk) might reduce the amplitudes of libration and eccentricity oscillations for systems such as this one. A case like the one illustrated in Fig. 12 is clearly not a typical outcome of purely dynamical evolution. We found a few other systems ($\sim 1\%$) showing similar librations of $\theta_{1,2}$ at different times during their dynamical evolution, but only for a brief phase never exceeding $\sim 10^4 T_{1,i}$. However, if our simulations had included even some weak dissipation, the frequency of such resonances might have increased significantly. We encourage future investigation of this possibility.

2.8. Mass Dependences

Our simulations show the effects of mass segregation, as heavier planets preferentially end with smaller semi-major axes. This trend can be easily seen by comparing the initial and final mass distributions of the planets in Fig. 13. The mass distribution clearly shifts towards higher mass values in the final inner planet mass histogram, whereas, the outer planet mass more closely re-

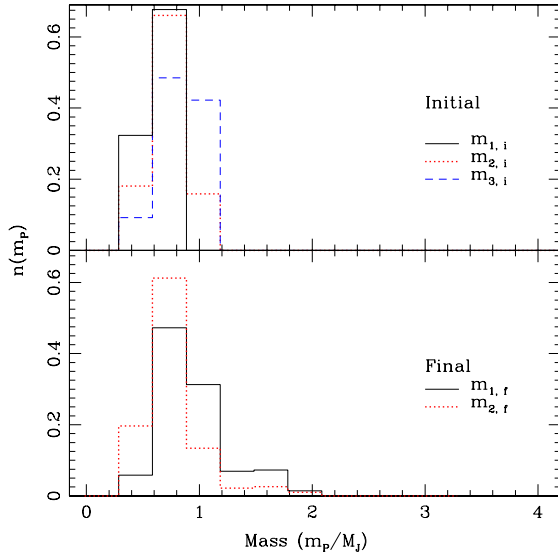


FIG. 13.— Initial and final mass distributions of the closest, middle and furthest planets. The top (bottom) panel shows the initial (final) mass distributions. Solid (black), dotted (red), and dashed (blue) lines in the top panel represent the initial mass histograms of the closest, middle, and furthest planets. Solid (black) and dotted (red) lines in the bottom panel represent the mass histograms of the final inner and outer planets, respectively. One planet is ejected in each of our simulations. Note that the histogram for the inner planet masses shifts towards higher values in the bottom panel, which indicates that the higher mass planets preferentially become the inner planet in the final stable configuration of the planetary systems.

flects the initial mass distribution (compare the top and bottom panels of Fig. 13). We do not find a strong effect of mass on eccentricity but we note that collisions tend to reduce the fraction of highly eccentric systems (Fig. 14). The collision products can be seen in the cluster around and above $1.5 M_J$. We find no other significant mass dependent effect in the final orbital parameters for our set of runs using Mass Distribution 1.

We now describe briefly the results obtained with the two alternative initial mass distributions for the three planets. Fig. 15 shows correlation between semi-major axis and mass for both Mass Distribution 1 (§2.2.1) and Mass Distribution 2 (§2.2.2). Somewhat surprisingly, for Mass Distribution 2, we find no significant differences from the results obtained with the much simpler prescription of Mass Distribution 1. This is possibly because in both Mass Distributions 1 and 2, the mass range and distribution are similar (Mass Distribution 2 is only shifted towards slightly higher values).

For this reason we also studied a third choice of mass distribution, Mass Distribution 3 (§2.2.3), with a much larger range of planetary masses, enabling us to observe mass-dependent effects more clearly. For example, we now see that the tendency for higher mass planets preferentially to become the final inner planets (Fig. 16) is more prominent than in our other simulations. Similarly, the effect of a mass distribution on the final eccentricities of the remaining planets is more prominent with this broader mass distribution. The higher-mass planets preferentially excite the eccentricities of the lower-mass counterparts, often to the point of ejection. This effectively reduces the overall eccentricities of the final stable orbits (Fig. 17). The median value of the final inner orbit

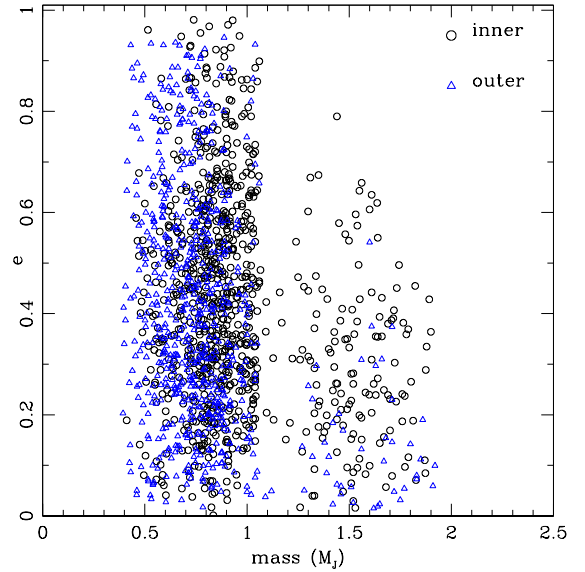


FIG. 14.— Mass vs eccentricity of the final stable planets. The circles (black) and the triangles (blue) represent the final inner and the outer planets. Planets with masses $\geq 1.6 M_J$ are collision products. The collision planets tend to have lower eccentricities.

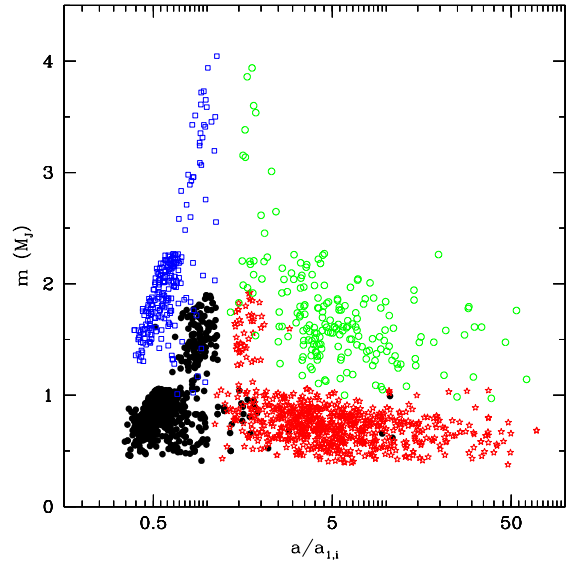


FIG. 15.— Mass vs semi-major axis of the final remaining stable planets. The disks (black) and the open stars (red) represent the final inner and the outer planets for Mass Distribution 1. The open squares (blue) and the open circles (green) represent the same, respectively, for Mass Distribution 2. Note, higher mass planets remain close to their initial positions.

eccentricities is 0.24, and that for the outer orbit is 0.23 in this case. The final cumulative distribution of eccentricities matches the observations even more closely with Mass Distribution 3 than with Mass Distribution 1 or 2 (Fig. 18; Table 1). We employ similar selection criteria as described in §2.5. The final semi-major axis distribution is statistically indistinguishable from the one obtained with Mass Distribution 1. We also clearly see that the lower-mass planets get scattered around preferentially while the heavier counterparts do not move much and stay mostly near their initial positions (Fig. 19). This is

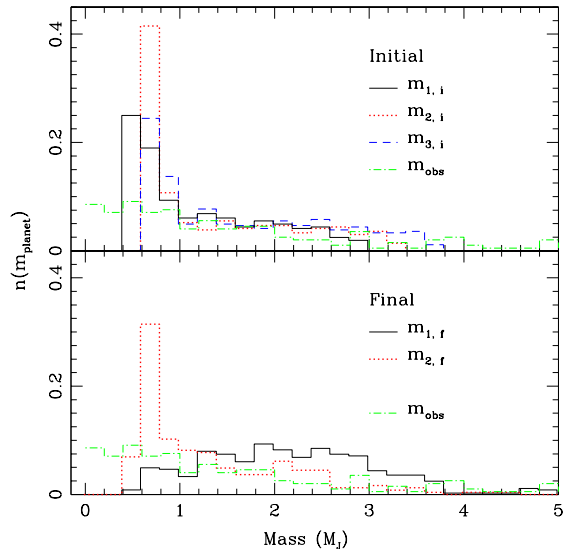


FIG. 16.— Same as Fig. 13, but with a different and wider initial mass distribution than the previous one (Mass Distribution 3). The initial mass distribution has a high number of Jovian mass planets as in the previous mass distribution, however, in this case the distribution has a tail towards higher masses. The higher end in the initial mass spectra in this case mimics the minimum mass ($m \sin i$) spectrum of the observed exoplanets. Note that the mass segregation effect is more prominent here than in Fig. 13. The dot-dash (green) line shows the $m \sin i$ distribution of the observed exoplanets in both panels for comparison.

in accord with the observation that close-in planets are often of lower mass than planets with moderate semi-major axes (Cumming et al. 2008; Naef et al. 2005). At present, the correlation between planet mass and orbital period for radial-velocity planets is consistent with a population of systems where the less massive planets have been scattered inwards. We predict that planet searches sensitive to longer-period planets will eventually find a population of sub-Jupiter planets that have been scattered outwards. Furthermore, our simulations predict a negative correlation between mass and orbital period among such long-period planets, if they are launched into their current orbits via strong gravitational scattering. We find that mass and eccentricity have a weak anti-correlation (Fig. 20). We do not find any systems with two planets trapped in 2:1 MMR for this case.

2.9. Secular evolution

It is known from numerous previous studies that secular perturbations of one planet on another in a multi-planet system can modify the planets’ orbital properties on a timescale much longer than the relevant dynamical (orbital, or strong dynamical instability) timescales (Adams & Laughlin 2006a; see also Murray & Dermott 2000). Since secular timescales can be orders of magnitude longer than the orbital timescales, one might obtain results biased towards the initial part of the oscillations if at least a full secular period is not sampled properly. Fig. 21 shows a dramatic example where the eccentricities of both planets and the relative inclinations between the planetary orbits oscillate secularly with a very long period (~ 100 Myr) compared to the orbital timescale and the observed eccentricities and inclinations can be very different from what would be expected right after dynamical stabilization of the system. Hence, any study

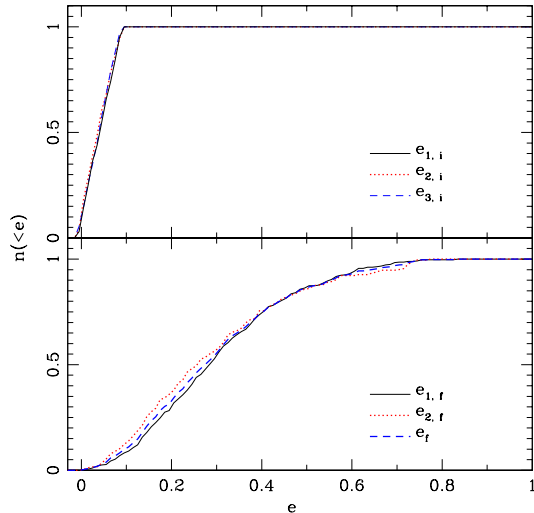


FIG. 17.— Same as Fig. 3, but using Mass Distribution 3. Note that overall the eccentricities are lowered using the broader mass distribution.

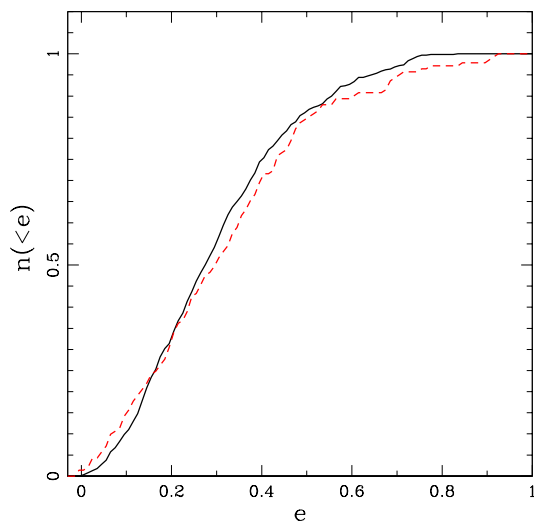


FIG. 18.— Same as Fig. 4, but using Mass Distribution 3. The simulated eccentricities match much better with the observed in this case compared to those using Mass Distribution 1.

of orbital properties of planets after dynamical interactions should also worry about the secular evolution of the orbital properties that follows the orders of magnitude quicker dynamical phase. Nevertheless, we should point out that in our simulated systems this is not typical. For most cases the secular time period is typically $\sim 10^5 - 10^6$ yr. For our simulated systems containing two provably stable planets at the end of our common integration stopping time (10^7 yr) we study the evolution of the eccentricities for a further 10^9 yr to confirm that the orbital properties at the end of our integration correctly represent the true final distribution.

To evaluate the secular evolution of these planets, we use the octupole-order formalism presented by Ford et al. (2000). Note that the more stan-

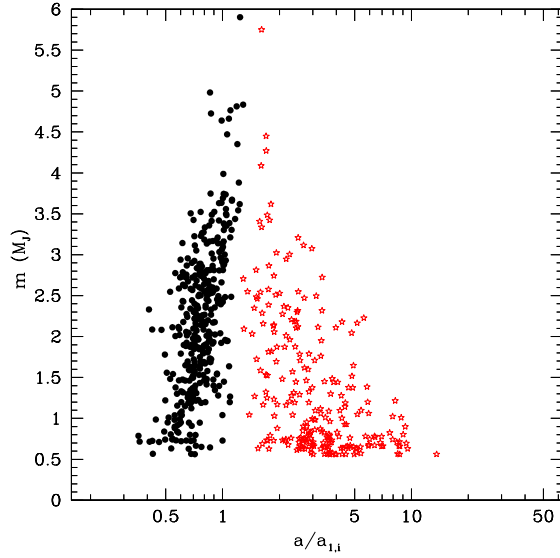


FIG. 19.— Same as Fig. 15, but using Mass Distribution 3. Mass dependent effects on final semi-major axes of the planets is much more prominent in this case.

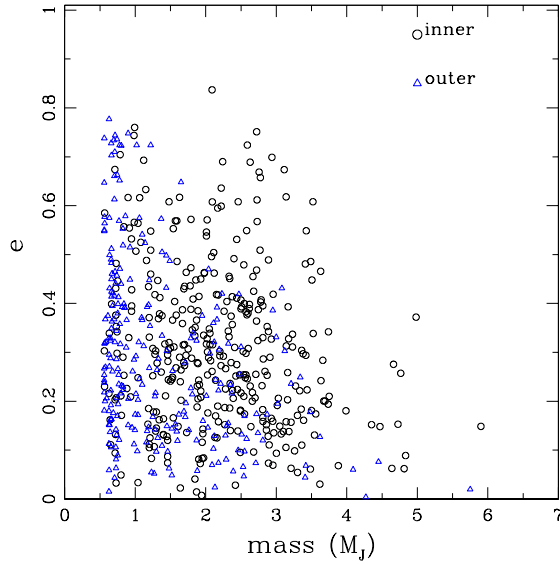


FIG. 20.— Same as Fig. 14, but using the broader distribution of initial planet masses (mass distribution 3). There seems to be a weak anti-correlation between the mass and the eccentricities of the planets.

dard formulation in terms of the Laplace coefficients (Murray & Dermott 2000) is not appropriate for these planetary systems because a significant fraction of these systems contain orbits with very high eccentricities and inclinations.

We find that indeed individual eccentricities of these planetary orbits can change significantly. Fig. 22 shows a scatter plot of the final eccentricities after secular evolution for 10^9 yr as a function of the eccentricities after our integration stopping time for both planets. It is clear that the individual eccentricities can change significantly, especially, for the inner planet. However, the overall distribution does not change significantly from the distribution obtained right after our integration stopping time in

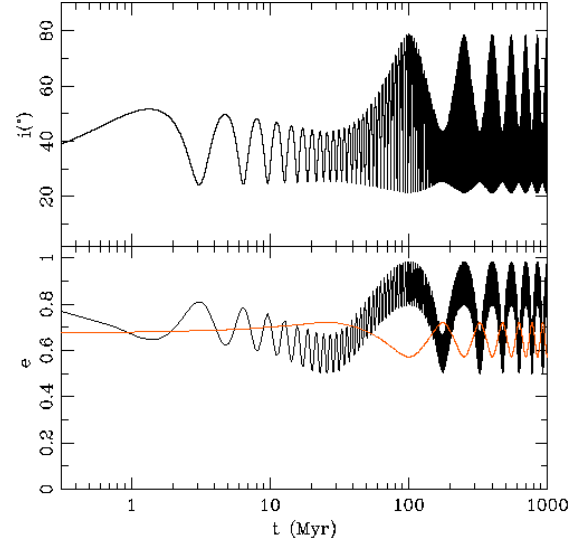


FIG. 21.— Secular time evolution of the relative inclination (top panel) and the eccentricities (bottom panel) of a system with two dynamically stable planets. $t = 0$ for this is the end of dynamical integration (§2.3). In the bottom panel the curve with a smaller oscillation amplitude (red) shows the evolution of the outer planet eccentricity and the other (black) shows that of the inner planet.

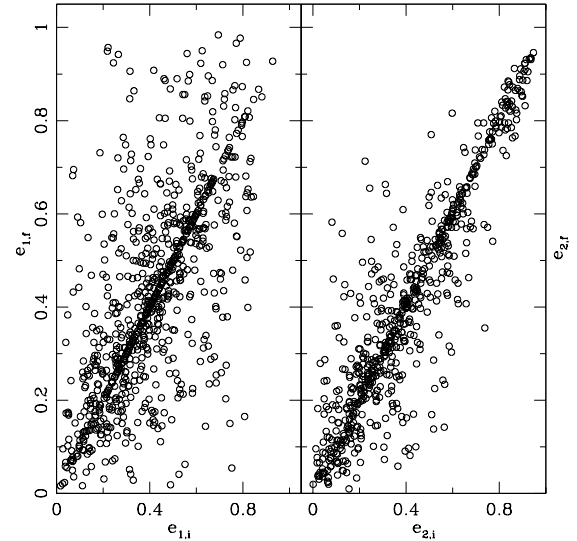


FIG. 22.— Scatter plot of eccentricity after secular evolution for 10^9 yr vs eccentricity after the integration stopping time (§2.3). Left and right panels show the inner and outer planets, respectively. Note that the eccentricities for the inner orbits change more significantly than for the outer ones.

§2.3. Fig. 23 shows that the eccentricity distributions before and after secular evolution for the outer planet, in particular, are statistically identical. For the inner planets we find that, after secular evolution, there is a little overabundance of very high eccentricity ($e \geq 0.8$) orbits (Fig. 23). In order to quantify the likeness of the two distributions before and after secular evolution, we perform KS tests for both the inner and outer planet eccentricity distribution. We find that we cannot rule out the null hypothesis (that the distributions before and after secular evolution are drawn from the same distribution) at 62% and 1% significance level for the inner and outer

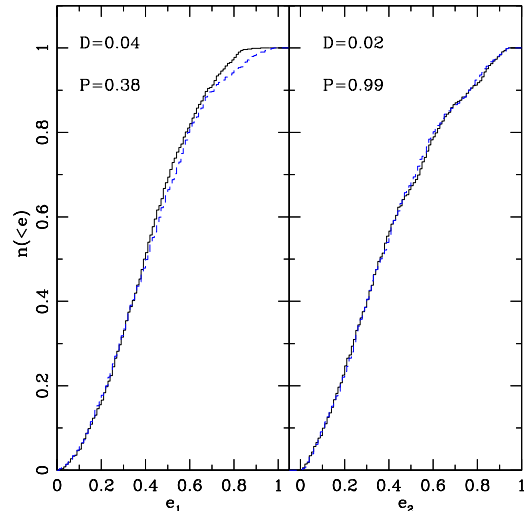


FIG. 23.— Left panel: Cumulative distributions of eccentricities of the inner planets before and after secular evolution described in §2.9. Solid (black) and dashed (blue) lines show the distributions before and after secular evolution, respectively. Right panel: Same as left panel, for the outer planet. KS test results for both pairs of distributions are also shown in the plot.

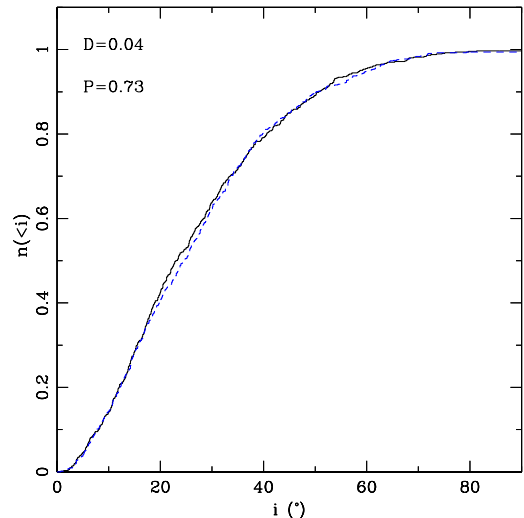


FIG. 24.— Left panel: Cumulative distributions of relative inclinations between the planetary orbits before and after secular evolution described in §2.9. Solid (black) and dashed (blue) lines show the distributions before and after secular evolution, respectively. KS test results for the two distributions (before and after secular evolution) are also shown in the plot.

planetary orbits, respectively. The very low values of the significance level along with the large ensemble essentially means that the two distributions are very similar. We perform the same test with the relative inclination of the planetary orbits in the subset of our systems with two dynamically stable remaining planets (Fig. 24). For these distributions the significance level for KS test with the same null hypothesis is 27%. This confirms that our choice of integration stopping time already sampled the full parameter space for the secular evolution.

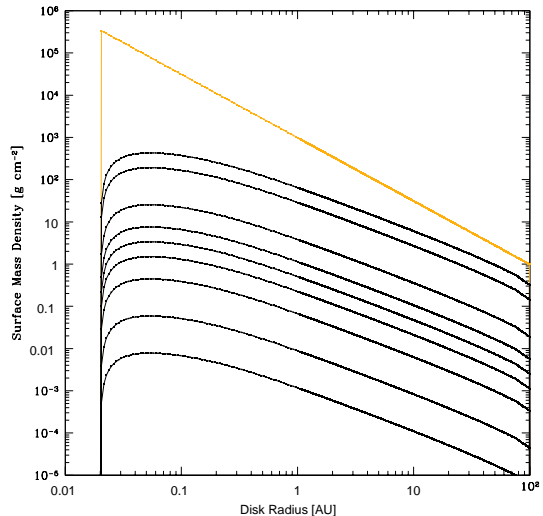


FIG. 25.— Surface mass densities for runs with DISK1–9 (black line). Also shown is the standard surface mass density $\Sigma = 10^3(r/\text{AU})^{-3/2}$ (yellow line). The surface mass densities for DISK1–9 are obtained by evolving a disk with the standard surface mass density under disk’s viscosity parameter of $\alpha = 5 \times 10^{-3}$ for 3, 5, 10, 13, 15, 17, 20, 25, and 30 Myr.

3. EFFECTS OF A RESIDUAL GAS DISK

In the previous section we considered the dynamical evolution of three-planet systems with fully formed planets on initially near-circular orbits and no gas disk. Implicit assumptions are that sufficiently massive disks damp planetary eccentricities, and that residual gas disks dissipate quickly enough to allow the later chaotic evolution of planetary systems. Here, we will verify these assumptions by simulating three-planet systems within residual gas disks.

3.1. Photoevaporation

The final stage of disk dissipation remains poorly understood. Since viscous evolution alone cannot explain the observed rapid dispersal of disks ($\sim 10^5$ yr; see e.g., Simon & Prato 1995), some other mechanism must be responsible for removing a residual disk. The most likely is photoevaporation (e.g., Shu et al. 1993; Hollenbach et al. 1994). Clarke et al. (2001) proposed that, once the viscous accretion rate drops to a level comparable to the wind mass loss rate, photoevaporation takes over the disk evolution. When this limit is reached, surface layers of the disk beyond the gravitational radius ($R_g = GM/c_s^2$), where the sound speed c_s exceeds the disk’s escape speed, starts removing disk mass faster than it is being replenished by viscous evolution. As a result, the disk is divided into inner and outer parts: the inner disk drains onto the central star on a short viscous timescale, while the outer disk evaporates on longer timescales (e.g., Clarke et al. 2001; Alexander et al. 2006). Alexander et al. (2006) showed that the disk clearing by this mechanism takes about 10^5 yr, which is comparable to the observed dissipation time.

The viscous evolution time at semi-major axis a is de-

finned as

$$t_{\text{vis}}(a) = \frac{M_{\text{disk}}(\leq a)}{\dot{M}_{\text{disk}}(a)} \quad (10)$$

$$\dot{M}_{\text{disk}} \simeq 3\pi\nu\Sigma, \quad (11)$$

where ν and Σ are the viscosity and surface mass density, respectively.

On the other hand, the photoevaporation time at a is

$$t_{\text{photo}}(a) = \frac{M_{\text{disk}}(\leq a)}{\dot{M}_{\text{wind}}(a)}, \quad (12)$$

where the wind mass loss rate for an optically thick disk is (Clarke et al. 2001)

$$\dot{M}_{\text{wind}} = 4.4 \times 10^{-10} \left(\frac{\Phi}{10^{41} \text{ s}^{-1}} \right)^{1/2} \left(\frac{M_*}{M_{\odot}} \right)^{1/2} M_{\odot} \text{ yr}^{-1}, \quad (13)$$

and for an optically thin disk (Alexander et al. 2006)

$$\dot{M}_{\text{wind}} = 9.68 \times 10^{-10} \mu \left(\frac{\Phi}{10^{41} \text{ s}^{-1}} \right)^{1/2} \left(\frac{h/a}{0.05} \right)^{-1/2} \left(\frac{a_{\text{in}}}{3 \text{ AU}} \right)^{1/2} \left[1 - \left(\frac{a_{\text{in}}}{a_{\text{out}}} \right)^{0.42} \right] M_{\odot} \text{ yr}^{-1} \quad (14)$$

Here Φ is the ionizing flux from the central star, h is the pressure scale height of the disk, a_{in} and a_{out} are the inner and outer disk radii.

Photoevaporation becomes effective when $t_{\text{vis}} \geq t_{\text{photo}}$. For typical disks, this corresponds to a disk mass of a few Jupiter masses. When a disk mass drops below this critical value, planets are likely to become dynamically unstable if the photoevaporation time is shorter than the dynamical instability growth time ($t_{\text{photo}} < t_{\text{dyn}}$). In this section we will investigate this further by simulating 3-planet systems with various disk masses.

3.2. Numerical Method and Assumptions

For this study we use a hybrid N -body and 1-D gas dynamics code to follow the evolution of three-planet systems for several different disk masses. Our hybrid code in its current form combines an existing N -body integrator with a 1-D implementation of a viscous, nearly Keplerian gas disk (Thommes 2005). The N -body code is based on SyMBA (Duncan et al. 1998). It is fast for near-Keplerian systems, requiring only ~ 10 timesteps per shortest orbit, while undergoing no secular growth in energy error. In addition, it makes use of an adaptive timestep to resolve close encounters between pairs of bodies.

The gas disk is divided into radial bins, each of which represents an annulus whose properties (surface density, viscosity, temperature, etc.) are azimuthally and vertically averaged, following the general approach of Lin & Papaloizou (1986). Arbitrary viscosities can be specified through a standard α -parametrization (Shakura & Syunyaev 1973). Though this disk is explicitly 1-D, the vertical and azimuthal structures are implicitly included in the model. For the former, a scale height is assigned to every annulus. The latter is key to the planet-disk interactions, which result from the raising of azimuthally asymmetric structure (spiral density waves) in the disk by the

TABLE 2
DISK MODELS

	Disk Mass	Disk Age (10^7 yr)	t_{damp} (10^6 yr)
DISK1	$3.7 M_J$	0.3	0.2 for 17/24
DISK2	$2.2 M_J$	0.5	0.4 for 14/23
DISK3	$0.22 M_J$	1.0	4 for 17/28
DISK4	$23.5 M_{\oplus}$	1.3	7 for 5/27
DISK5	$11.8 M_{\oplus}$	1.5	-
DISK6	$4.7 M_{\oplus}$	1.7	-
DISK7	$1.4 M_{\oplus}$	2.0	-
DISK8	$0.19 M_{\oplus}$	2.5	-
DISK9	$0.02 M_{\oplus}$	3.0	-

^a The disk masses of the 9 different disk models used in §3. The disk age is the time until a typical disk with $\alpha = 5 \times 10^3$ will reach the corresponding total mass. The eccentricity damping time is the time to reduce the planetary eccentricities from above 0.1 to below 0.1, and obtained for systems which did not go through mergers.

planet. This effect is added in the form of the torque density prescription of Goldreich & Tremaine (1980), as modified by Ward (1997), which describes the disk-planet angular momentum exchange taking place as waves are launched. Planetary eccentricities are damped on timescales as in Ward (1993) and Artymowicz (1993). Since we do not take account of the saturation of corotation resonances, which could lead to the eccentricity excitation by Lindblad resonances (Goldreich & Sari 2003; Moorhead & Adams 2008), the eccentricity damping considered here is an upper limit.

3.3. Results: Onset of Dynamical Instability

For initial conditions, we randomly choose 30 three-planet systems from the set using Mass Distribution 1 in §2.2.1, and study their orbital evolution within 9 different disk masses. The surface mass density profiles of these disks are shown in Fig. 25. These are obtained by evolving a minimum mass solar nebula disk model with a viscosity parameter $\alpha = 0.005$ for various times (without planets). Disk properties are summarized in Table 2, and we will refer to our models as DISK1-9 from here on. We assume that each of these disks is *inviscid* for dynamical runs with planets, meaning that type II planet migration is not taken into account. However, this should not affect our results significantly since even the most massive disk (DISK1) contains only $3.7 M_J$, which is comparable to the planetary masses used in our simulations. Most of our disks are therefore too small to affect planet migration.

The dynamical instability is commonly characterized by the orbital crossings of planets. Fig. 26 shows the first orbital crossing time of each system for each disk mass. Diagonal lines are disk clearing timescales by photoevaporation for optically thick disks (orange/grey lines), and optically thin disks (blue/black lines). Also plotted is the viscous evolution times at the gravitational radius. This figure indicates that photoevaporation takes over disk evolution for disks with a few to several Jupiter masses, depending on the photoevaporation models.

It appears that the range of first orbital crossing time t_{dyn} is relatively independent of disk masses, and around $\sim 10 - 10^4$ yr. Note, however, that the number of systems going through orbital crossings decreases for larger disk masses. Excluding mergers, 19/24, 14/28, and 4/28 sys-

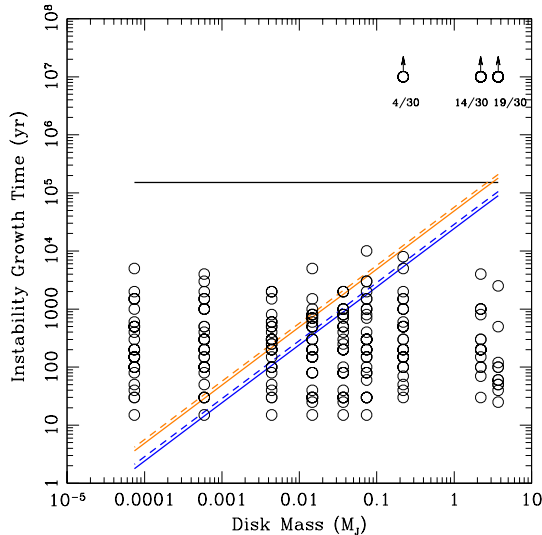


FIG. 26.— Instability growth timescale for 30 planetary systems with DISK1-9 (from right to left). The range of dynamical instability time is relatively independent of disk masses. Data points with an arrow indicate the number of systems which did not go through dynamical instability within our simulation time ($\sim 10^7$ yr). Diagonal lines are disk clearing times by photoevaporation for optically thin disks (dark lines) and optically thick disks (light lines). Solid and dashed lines are the disk clearing time measured at the gravitational radius R_g and 10 AU respectively. The horizontal line shows the viscous evolution timescale of the disk at R_g . Photoevaporation is expected to take over disk evolution once $t_{\text{viscous}}(R_g) \sim t_{\text{photo}}(R_g)$. Planetary systems are likely to go through a chaotic evolution as shown in gas free systems (§2) when $t_{\text{photo}} < t_{\text{dyn}}$ (i.e. above t_{photo} lines in the figure).

tems for DISK1, 2, and 3, respectively do not experience any orbital crossings during the simulation time (10^7 yr), while all systems with lighter disk masses go through at least one crossing within the run time. This is concordant to expectations that planets become dynamically unstable more readily in a less massive gas disk and the same planetary system that remained stable in a sufficiently massive disk can become unstable once the disk dissipates.

Apart from t_{dyn} , the eccentricity damping timescale (t_{damp}) is very important to know, since t_{damp} determines whether the disk can damp the eccentricities back to near zero after one (or more) orbit-crossing episode(s), before the disk is depleted. We define t_{damp} as the time taken to damp the planetary eccentricities from $e > 0.1$ to $e < 0.1$. For 30 different systems for 4 disk masses (DISK1-4) we find the median t_{damp} to be 2×10^5 , 4×10^5 , 4×10^6 , and 7×10^6 yr, respectively. For less massive disks we do not find significant damping. While the evolution of disks is dominated by viscous evolution and $t_{\text{damp}} < t_{\text{vis}}$ (DISK1 and 2), planetary orbits are expected to remain nearly circular since after an instability there is enough time to damp the eccentricities before the disk is depleted. The nature of evolution can change drastically once photoevaporation dominates the disk evolution and starts depleting the disk more rapidly. We find that most systems reach at least one orbit-crossing episode for the least massive disks (DISK8 and 9) since $t_{\text{dyn}} > t_{\text{photo}}$. Some planetary systems in more massive disks have $t_{\text{dyn}} < t_{\text{photo}}$ (Fig. 26). For these more massive disks eccentricities

excited via planet-planet interaction may be damped if $t_{\text{damp}} < t_{\text{photo}}$. However, since the median t_{damp} is longer than t_{photo} for these disks, planetary eccentricities excited via planet-planet interaction do not have time to be damped before the gas disk is depleted, once photoevaporation is efficient.

In summary, we expect that planetary systems will remain stable with nearly circular orbits while the planets are embedded in a sufficiently massive disk. Even if there is an occasional orbital crossing or merger, the eccentricities and inclinations will rapidly damp in such a disk, so that the system returns to nearly circular orbits. Then eccentricities will evolve more freely once photoevaporation takes over the disk evolution, and the disk clearing time becomes short compared to the instability growth time ($t_{\text{dyn}} > t_{\text{photo}}$). Even when planets become unstable before the disk is completely depleted ($t_{\text{dyn}} < t_{\text{photo}}$), it is unlikely that their eccentricities are damped, since the eccentricity damping times of these disks tend to be longer than the disk dissipation time ($t_{\text{damp}} > t_{\text{photo}}$). Therefore, we expect that most planetary systems become dynamically unstable when a gas disk dissipates. This further justifies our initial conditions in §2. In a future paper we will further investigate the evolution of multiple-planet systems within an evolving gas disk (Matsumura et al. 2008).

4. COMPARISON WITH PREVIOUS STUDIES

The previous work most similar to ours was the pioneering study by MW02 on (gas-free) three-planet systems. MW02 also studied the orbital properties of planetary systems following a dynamically active phase of their evolution. However, their study was computationally limited and their systems were rather idealized in terms of assumed planetary masses and initial orbits. Our results are in good qualitative agreement with those of MW02. For example, they showed for the first time with three-planet systems how scattering can produce large eccentricities. However, our more realistic and generalized initial conditions enable us to explore a larger parameter space and to study in more detail the most interesting phenomena such as the generation of large, potentially observable inclinations. We also find that the final stable planets can be scattered at even smaller semi-major axes than they predicted. Since these very low semi-major axes planets are in the tail of the distribution, it is expected that a simulation of a smaller sample size will miss some of them (see Appendix A). Moreover, our much larger simulated sets and improved statistics on dynamical outcomes allow us to better compare our theoretical predictions to observations (see Appendix A).

In addition to the orbital properties of remaining planets, MW02 also presented a stability timescale analysis for planetary systems with three giant planets. In verifying these results, we realized the importance of this study, especially for our choice of initial spacing, and we therefore decided to perform a much more detailed timescale analysis, with significant improvements over MW02 made possible by the dramatically increased speed of present-day computers. The results of this analysis are presented in Appendix B.

Moorhead & Adams (2005) studied in detail two-planet systems with an empirical dissipation arising from a residual disk. They found that, even in initially well

separated two-planet systems, migration can bring the planets close enough for dynamical instability. In their study they accounted for a disk outside both planets with their empirical formula, whereas, we immerse the three planets in a protoplanetary disk with varying disk masses (§3). Another major difference between their study and ours is the number of planets considered. The dynamical evolution of two-planet systems can be very different from that of systems with three or more planets (see §1). Keeping these differences in mind, we compare key points between the two studies. For example, for sufficiently massive disks we find that the eccentricity damping timescale is less than the disk dissipation timescale. However, as the disk mass is diminished, the timescale for eccentricity damping and the number of unstable systems increases. They also find that scattering fills up the a - e plane for the inner planet orbit. Due to the setup of their initial conditions and the dynamical limitations of two-planet system they do not find planets with large orbital periods, normally produced by strong scattering between planets. They also stop integrating after 1 Myr or when the system has only one planet left. One should remember that in cases where two planets are remaining, the planetary properties can still change either through dynamical scattering (see discussion in §2.3) or even for dynamically stable systems, through long term secular perturbations (for a detailed discussion see §2.9).

More recently Juric & Tremaine (2007) perform an interesting study as an extension of the pioneering work by Lin & Ida (1997). They study the dynamical evolution of generic N -planet systems with $N \geq 3$ and a wide range of initial conditions. Although their three-planet systems were dynamically inactive as a result of their choice of initial separations and integration stopping time, their other runs with higher N bear very relevant results for our study. In particular, they find a similar final eccentricity distribution, suggesting that this distribution may be universal. One of the most interesting results in their study is that the final number of surviving planets following a dynamically active phase is almost always 2–3, independent of the initial number. Since these systems are chaotic, the properties of any planetary system emerging out of a dynamically active phase will have little memory of the initial number of planets or the exact initial conditions (also see discussion in §2.4 and §2.6). One can imagine a situation where a system started with $N > 3$ and, followed by many collisions and ejections, reaches a stage with $N = 3$. If dissipation circularizes orbits after each ejection or collision, then such a system could reach a state similar to the initial conditions for our three-planet simulations. Thus, our results may be representative of even more generic multi-planet systems.

Nagasawa et al. (2008) study the dynamics of three *equal-mass* planets including dynamical tides. Since they can apply tides while the three-planet dynamical scattering phase is still active, they find increased efficiency to tidally isolate planets that would otherwise still actively take part in three-planet scattering. In this study we did not include tides. However, we find that 8% of these systems have one planet accreted onto the star. We also find that $\sim 40\%$ of these systems contained at least one planet which, during the three-planet violent scattering phase, reached a pericenter distance within 0.01 AU of the star. In most of the systems these close-in planets end up be-

ing ejected, while, some of them collide with the star or another planet. None of these systems remain stable at the end of the run. The addition of tides during these scattering phases may stabilize some systems by isolating the close-in planet from the other planets dynamically. Of course the circularization process needs to be very efficient and quick so that the planet gets circularized and decoupled from the others before it can be ejected. We should also point out that Nagasawa et al. (2008) study *equal-mass* planets. We find that the dynamical evolution of planetary systems with unequal masses is very different than for equal mass systems (see discussion in §2.2 & §2.8). In particular, the lower-mass planets preferentially get scattered inwards or outwards while the heavier counterparts remain near their initial positions throughout the whole evolution (e.g., see Fig. 15). One should also remember that the tidal circularization timescale depends on the mass and radius of these planets (e.g., Ivanov & Papaloizou 2004). This can affect the efficiency of tidal circularization for high eccentricity planets in their setup. At present their study actually produces too many (30%) “hot” planets compared to the current observed population of $\sim 5\%$ within 0.03 AU (at 0.03 AU the tidal circularization timescale is $\sim 10^6$ yr for Jovian planets, see Nagasawa et al. 2008). Note that the selection biases of radial velocity surveys can only reduce the fraction of hot Jovian planets in the future. It will be interesting to see results of similar studies with a more realistic mass distribution.

5. SUMMARY AND CONCLUSIONS

We have studied in detail how the orbital properties evolve through strong gravitational scattering between multiple giant planets in a planetary system containing three giant planets around a solar mass star. We perform a detailed study for gas free generic planetary systems. We focus on the final orbital properties of the planets that remain bound to the central star in stable orbits after chaotic evolution due to strong mutual interactions, followed by a prolonged secular evolution ($\sim 10^9$ yr) when two planets remain after the scattering phase. We perform the experiments with realistic planetary systems containing 3 giant planets (§2). In all of these systems at least one planet is eventually ejected before reaching a stable configuration. This supports models of planet formation that predict planetary systems initially form several closely spaced planets, but instabilities reduce the number of planets until the stability timescale exceeds the age of the planetary system. In 20% of the cases, two planets are lost through ejections or collisions leaving the system with only one giant planet. Thus, the planet scattering model predicts the existence of many systems with a single eccentric giant planet, as well as many free floating planets (depending on how many planets are formed before the planet scattering phase of evolution).

We find that strong gravitational scattering between giant planets can naturally create high-eccentricity orbits. The exact distribution of eccentricities for the final remaining planets in stable orbits depends on the choice and range of the initial mass distribution. When the initial mass distribution spans a broad range of masses, the less massive planets typically start to acquire larger eccentricities. However, these planets with highly excited

orbits are often ejected, reducing the overall eccentricities of the remaining dynamically stable planetary orbits. Although the first two sets of our models (with a narrower range of initial planet masses) predict eccentric planets to be slightly more common than observed (Fig. 4), a wider initial mass distribution can result in remarkable similarity with the observed distribution (Fig. 18). Recently, a similar trend in eccentricities was found independently by Juric & Tremaine (2007) for generic dynamically active multi-planet systems independent of the details of the initial conditions or the initial number of planets.

We conclude that planet–planet scattering could easily account for the observed distribution of eccentricities exceeding 0.2. However, our simulations slightly underproduce systems with eccentricities less than 0.2. This may suggest that some observed systems are affected by late stage giant collisions. Alternatively, the presence of a residual gas or planetesimal disk could lead to eccentricity damping. We find this latter explanation particularly attractive given the observed correlation between planet mass and eccentricity (Butler et al. 2006). While our simulations suggest that high eccentricities are most common among less massive giant planets, the known population of extrasolar planets suggest that high eccentricities are more common among the more massive planets (Ford & Rasio 2007). This apparent discrepancy could be resolved if a modest disk often remains after the final major planet–planet scattering event. Less massive planets would be more strongly affected by the remaining disk, so their eccentricities could be damped, while more massive planets would typically be immune to eccentricity damping.

We find that it is possible to scatter some planets into orbits with low perihelion distances (Fig. 8). Approximately 10% of the systems obtain perihelion distances less than $0.05 a_{1,i}$, whereas, a fewer fraction ($\sim 2\%$) can reach within $0.01 a_{1,i}$. If the initial semi-major axes are small enough, then strong gravitational scattering could result in planet orbits with sufficiently small perihelion distances, such that tidal effects could circularize their orbits at small orbital distances.

We find that the inclination distribution of such planets could be significantly broadened. If we assume that the angular momentum of the host star is aligned with that of the initial orbital angular momentum of the planets, then measurements of λ (the angle between stellar spin axis and planet’s orbital angular momentum) should typically be small in absence of perturbations from other planetary or stellar companions (§2.6). We find that strong gravitational scattering between the giant planets can naturally increase the inclinations of the final planetary orbits with respect to the initial total orbital angular momentum plane (Fig. 9). Since the timescale to tidally align the stellar spin and the planetary angular momentum is much greater than the age of the star ($\sim 10^{12}$ yr; Greenberg 1974; Hut 1980; Winn et al. 2005), inclinations excited by planet–planet scattering after the disk had dispersed could be maintained for the entire stellar lifetime. Observations of a hot-Jupiter with a significantly non-zero λ would be suggestive of previous planet–planet scattering. However, caution would be necessary if the star had a binary stellar companion (Wu & Murray 2003; Takeda & Rasio 2005; Fabrycky & Tremaine 2007). On the other hand,

observations of many hot-Jupiters with orbital angular momenta closely aligned with their stellar rotation axis would suggest a formation mechanism other than strong gravitational scattering followed by tidal circularization. Unfortunately, current observations measure this angle for only a few systems and some measurements have uncertainties comparable to the dispersion of inclinations found in our simulations. We encourage observers to improve both the number and precision of Rossiter–McLaughlin observations.

We find that the relative inclinations between planetary orbits in the systems with two remaining planets in their final stable orbits also increase via planet–planet scattering. Future observations using astrometry or transit timing could possibly measure relative inclinations between planetary orbits in multi-planet systems. Furthermore, we find that in $\sim 20\%$ of the systems having two giant planets in their final dynamically stable configurations, the relative inclination between the two planets is higher than 40° . For these systems it is possible for the planets to go through Kozai-type oscillations (Nagasawa et al. 2008). Although effects of a debris disk on planetary dynamics and vice versa is beyond the scope of this study, the warped disk observed in β Pictoris could be one interesting example where inclined planetary orbits and the debris disk exchange torques, resulting in a warped debris disk (Smith & Terrile 1984; Heap et al. 2000). Mouillet et al. (1997) suggests that the observed asymmetry in the debris disk can be explained by the presence of a planetary companion in an inclined orbit. Strong planetary scattering, as we find, can be a natural way to create planetary orbits with large semi-major axes and highly inclined orbits.

Less massive planets are more likely to be scattered far away from the site of their formation. Our simulations show that both the close-in or farther out planets should have lower mass than the planets with moderate semi-major axes (Figs. 15, 19). This trend can be verified in future observations using adaptive optics to detect and image giant planets further out (40–100 AU) from the central star (Lafrenière et al. 2007). We find that a few percent of the simulated population have very high semi-major axes in the final stable configuration (e.g., Fig. 6). Such giant planets are extremely unlikely to be created *in situ*, since the timescale for planet formation greatly exceeds the age of the star (Veras & Armitage 2004). Additionally, there is simply insufficient disk mass to form a giant planet at such large orbital distances (Kokubo & Ida 2002; Ida & Lin 2004b,a). Strong scattering between planets in multi-planet systems can be a natural mechanism to create such long-period planets ($a > 50$ AU). Our simulations suggest that this population of high semi-major axis planets will have high eccentricities and inclinations (Fig. 6). Future planet searches using astrometry or direct detection can test these predictions.

We have also presented a preliminary study of the effects of a residual gas disk on planetary dynamics (§3). We compare the importance of dynamics for 9 different disk models with different disk surface densities, keeping the initial orbital properties of the embedded planets the same for all cases. We identify important timescales for the dynamical evolution of these systems. In particular, we characterize the transitional stage of the dy-

namical evolution from the stable, eccentricity damped phase, where the planets are embedded in a massive disk to the unstable free eccentricity evolution stage following disk depletion. We show that it is possible to understand the overall evolution after planets are fully formed as an interplay between four different timescales, namely: the viscous timescale (t_{vis}) of the disk, the photo-evaporation timescale (t_{photo}) of the disk, the dynamical instability timescale t_{dyn} for the planetary orbits, and the eccentricity damping timescale (t_{damp}) for the planetary orbits in a disk (§3.3). Our study clearly shows that planets will remain stable on nearly circular orbits while a sufficient amount of gas remains present in the disk, while with the same initial orbits without gas the system would become unstable. The boundary between these two different phases can be characterized by t_{damp} , t_{vis} , and t_{photo} . The unstable phase starts when gas mass is sufficiently depleted so that $t_{damp} > t_{photo/vis}$. We find that the transition within a disk from a small to a large t_{damp} can be fairly quick once $t_{photo} < t_{vis}$ (Fig. 26). After photo-evaporation takes over the disk evolution, the sys-

tem undergoes a quick transition. Until the critical mass for photo-evaporation is reached, planetary eccentricities remain close to zero independent of the disk mass and previous dynamical history. Then, once the critical density is reached, the system behaves as if it had started with near-circular initial planetary orbits in a gas-free environment. Thus, apart from highlighting the relative importance of these timescales for the evolution of planetary systems, our results justify typical initial conditions used in most studies of gas-free multi-planet systems, including our own (§2). The initial properties for a gas-free system would be the orbital properties of the system as found at the boundary where $t_{damp} > t_{photo/vis}$, in this context.

This work was supported by NSF Grant AST-0507727 at Northwestern University. Support for E.B.F. was provided by NASA through Hubble Fellowship Grant HST-HF-01195.01A awarded by the Space Telescope Science Institute, which is operated by the Association of Universities for Research in Astronomy, Inc., for NASA, under contract NAS 5-26555.

APPENDIX

SAMPLE SIZE NEEDED TO ACCURATELY CHARACTERIZE THE ECCENTRICITY DISTRIBUTION

Due to the chaotic nature of n-body integrations and finite precision of computer arithmetic, the long-term integration of an exact system is impossible. Instead, we must perform ensembles of n-body integrations and interpret the results in terms of the statistical properties of the outcomes of a set of similar n-body systems. Given that any study is based on a finite sample size, it is important to recognize the limitations on the precision of various statistics due to the limited number of integrations. In the context of this paper (and similar works) many simulations of similar planetary systems are performed to generate a random sample of outcomes, each of which can be compared to the observable properties, such as the eccentricity and the semi-major axis of extrasolar planetary systems. Here we present an analysis of precision of several statistics describing the eccentricity distribution as a function of the number of n-body integrations performed. Formally, our estimated precision is applicable only to our specific choice for the distribution of initial conditions. Since this and previous studies have shown that many variations of the planet-planet scattering model result in similar eccentricity distributions, we expect that our results can be applied to many similar studies to estimate the accuracy of various statistical properties. Our results should also give a quantitative way to decide the required number of simulations to estimate various statistical properties to a given precision, and we expect this will be of use to other researchers when formulating research plans. Since the eccentricities of the planetary systems are one of the most interesting properties, we focus our attention on statistics describing the distribution of final eccentricities. However, the basic idea can be applied to any statistic describing the masses or orbital properties of the simulated planetary systems.

We will estimate the precision of several interesting statistics (the mean, the standard deviation, the 5th ($P5$) and the 95th ($P95$) percentiles of the distribution of final eccentricities). We estimate the “true” value for the underlying population based on estimates obtained making use of our full sample of $N = 1515$ simulations (see §2). We then estimate the same statistics based on m subsets of the full sample, where each subset is a random sample of n systems. Next, we compare the statistic estimated from each subset of simulations to the statistic based on the full population. We systematically change the sample size n for each subset, so as to explore how precisely we can estimate a given statistic as a function of the sample size.

In Fig. 27, we show each estimate for a given statistic as a single tick mark. Each panel presents results for a different statistic: mean (left, top), standard deviation (left, bottom), $P95$ (right, top), and $P5$ (right, bottom) of the eccentricity distribution. For each of the above statistics, we show the mean plus and minus the standard deviation (blue short dashed curves) and the 5th and 95th percentiles (magenta long-dashed curves). Hence, the upper magenta curve of the upper left panel shows the $P95$ for the estimate of the mean eccentricity based on a sample of $m = N/n$ estimates of the mean eccentricity each using a sample size of n . We find that for $n = 50$ the standard error in estimating the population mean from the sample can have a standard error of 37%, whereas, for $n = 100$ the precision improves to 5% (Fig. 27). In estimating the standard deviation of the eccentricity from the small subsamples, we find that with $n = 100$ the standard error in the estimation of the standard deviation of the eccentricity distribution is $\sim 7\%$ (Fig. 27). Although estimates for first two moments of the eccentricity distribution can come within 10% of the population moments based on only $n \geq 100$, a much larger sample size is required to characterize the tails of the eccentricity distribution accurately. For example, the errors in estimating the $P5$ and the $P95$ of the underlying eccentricity distribution using sample sizes of $n = 100$ are 30% and 7%, respectively. If the sample size is increased to $n \sim 1000$, then $P5$ and $P95$ can be estimated within 4% and 1% error, respectively.

Both previous and future studies often generate predictions for the eccentricity distribution of planetary systems

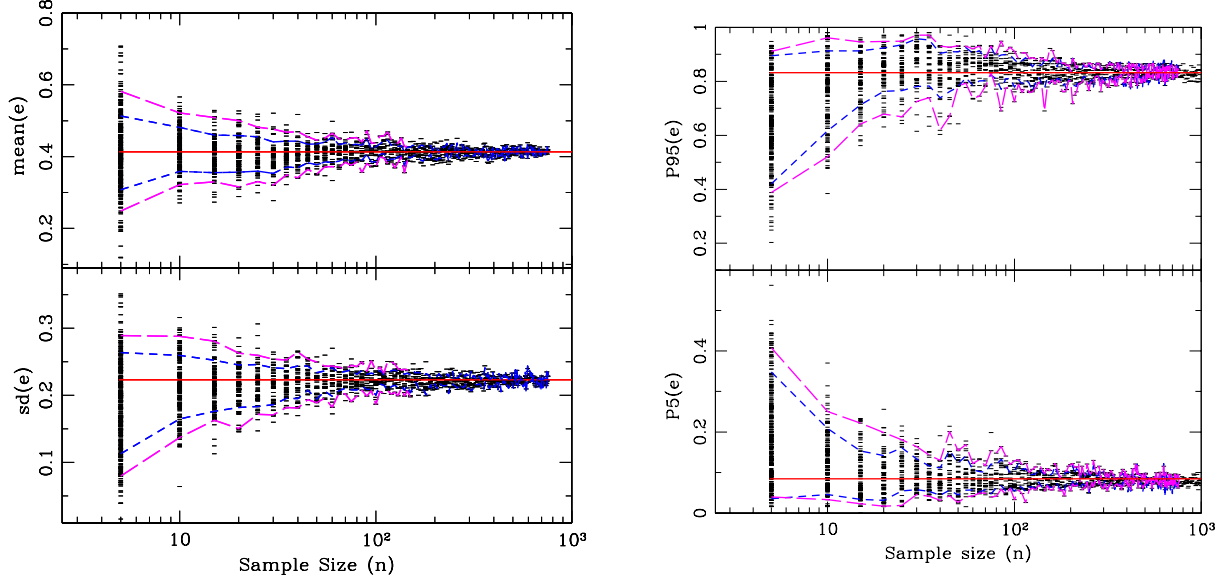


FIG. 27.— *Top left panel:* Each dash shows the mean eccentricities estimated from randomly chosen samples of sizes n , specified by the x-axis. The solid (red) line shows the mean eccentricity of the full sample. The short dashed (blue) lines show the standard deviation in the estimates of the mean eccentricity with respect to the full population mean for each sample size. The long dashed (magenta) lines show the 5th and the 95th percentiles of the estimates of the mean eccentricities. *Bottom left panel:* The same for the estimates of the standard deviation for the eccentricities. *Top right panel:* The same for the estimates of the 95th percentiles for the distribution of eccentricities. *Bottom right panel:* The same for the estimates of the 5th percentiles for the distribution of eccentricities.

based on various theoretical models. For the sake of comparing the precision with which these studies estimated the predicted eccentricity distribution, we have used the above result to obtain an empirical relation between the standard deviation of the estimates of various summary statistics describing the eccentricity distribution and the number of simulations used to estimate the statistic (Fig. 28). We expect that this relation will also be useful for planning future studies, where researchers will want to make a deliberate choice regarding the number of simulations and other simulation parameters such as length of integration time, number of particles, and inclusion of additional physics. We find that the standard deviation in the deviation of the estimated mean eccentricity from the population mean eccentricity decreases as a power law of sample size n with an index of -1.586 ± 0.004 . The standard deviation estimating $P5$ and $P95$ decreases less steeply with n ; here the power law indices are -0.58 ± 0.05 and 0.51 ± 0.03 , respectively. (These empirical relations are valid only for $n \geq 5$.) For example, a study that uses 100 simulations would typically estimate the mean of the predicted eccentricity distribution to within $\simeq 0.008$. However, a larger number of simulations becomes increasingly important for estimating the tails of the eccentricity distribution precisely. For example, an ensemble of 100 simulations typically estimates the $P5$ or the $P95$ with a precision of $\simeq 0.025$ or $\simeq 0.045$, respectively.

STABILITY TIMESCALE

According to the core accretion model of planet formation, planets form in a protoplanetary disk separated by a small number of Hill radii away from each other (Kokubo & Ida 1998, 2002). Hence, it is very interesting to have a good and statistically reliable investigation of the stability timescales as well as the distributions of the timescales as a function of the planet-planet distances in multiples (K) of their mutual Hill radii. A similar timescale study was also performed by Chambers et al. (1996). However, their study covers a very different range of planetary masses. The large ensembles used by our study not only produce a better statistical characterization of these timescales as a function of K , they also enable us for the first time to show the actual nontrivial shapes of these distributions. The actual distributions of these timescales for a given K value are particularly interesting for anyone performing a similar study and trying to decide upon a reasonable initial planetary separation, since due to the broad range, the computational effort needed will be determined by the few unusually stable realizations rather than the more frequent ones where instability can grow orders of magnitude quicker. For better comparison with MW02 we put the planet closest to the star at 5 AU and then determine the semi-major axes of the other two planets as follows,

$$a_{i+1} = a_i + K R_{H,i,i+1}, \quad (\text{B1})$$

where K is the spacing measured in terms of $R_{H,i,i+1}$, the mutual Hill radius for the i^{th} and $i+1^{\text{th}}$ planets,

$$R_{H,i,i+1} = \left(\frac{M_i + M_{i+1}}{3M_\star} \right)^{1/3} \frac{a_i + a_{i+1}}{2}, \quad (\text{B2})$$

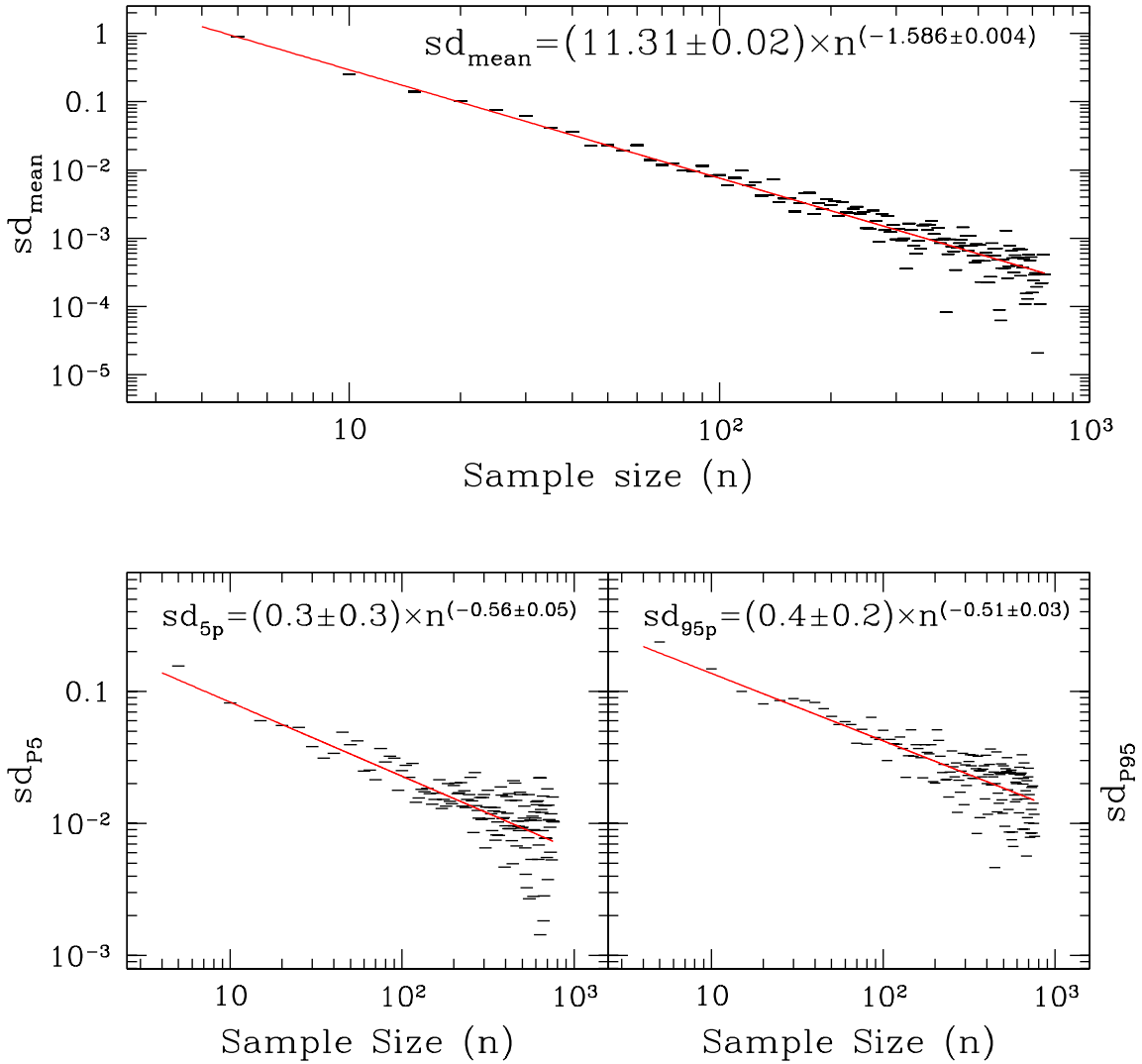


FIG. 28.— Standard deviations in the estimates of the mean (top panel), the 5th percentile (bottom left panel), and the 95th percentile (bottom right panel) for the eccentricity distribution based on a randomly chosen sample of size n . The solid (red) lines show the empirical fit for the standard deviation of the estimation of the statistic of interest as a function of the sample size. The empirical formulae for the fitting lines are also shown at the top of each panel. Note that the fits are only valid for samples of size greater than 5. Moreover, the standard deviation in the estimates for very large n (and hence very small standard deviation) is limited by the precision of our main simulated data (and is the reason for the saturation seen in the standard deviation values near $n = 1000$).

following their prescription. Here M_i is the mass of the i^{th} planet, M_* the mass of the central star, and a_i the semi-major axis of the i^{th} planet. Note we use a different definition of Hill radius from that in §2.2 following MW02 for easier comparison.

We integrate a number of 3-planet systems with different initial conditions: 1000 for $K \leq 4.3$, 500 for $4.3 < K \leq 5.0$ and 200 for $K \geq 5.0$. Apart from the large number of realizations, we use a more general distribution of the initial eccentricities and orbital inclinations as described in §2.2.

Fig. 29 shows the results as a function of K . The filled circles show the median and the vertical bars above and below represent $\pm 34\%$ around the median. Note that the vertical bars are not error bars, but they are representative of the actual distributions of the stability timescales. We also show the mean of each distribution to compare it with the median. In each case the mean overestimates the timescale and lies often outside the 34% bars around the median. Our results are consistent with the findings of MW02 qualitatively. We see similar trends near a MMR. However, we find that a simple linear fit as was tried by MW02 does not work well. A better empirical fit is given as follows.

$$\log_{10} t_m(K) = a + b \times \exp(cK), \quad (\text{B3})$$

where a , b , and c are constants (henceforth, called Fit-1). The best fit values for a , b , and c (Table 3) can predict the median timescales with fractional error less than 10% away from MMR. We also tried to find a simpler linear fit

TABLE 3
FIT: t vs K

	a	b	c	Max Error(%)
Fit 1	1.07	0.03	1.10	10
Fit 2	-1.74	1.29		50

^a The best fit values of the fitting parameters for the empirical fits for the median stability timescale of the systems as a function of their initial spacing parameter K .

$t_{m,linear}(K)$ for our data away from MMR, following MW02, writing

$$\log_{10} t_{m,linear}(K) = a + bK, \quad (\text{B4})$$

where a and b are fitting parameters (henceforth, called Fit-2). The best fit values for a and b are also given in Table 3. We find that Fit-1 is much better than Fit-2. In particular, we find that linear fitting formula for instability timescale as a function of initial spacing (as suggested by MW02) is inaccurate by over three orders of magnitude for initial spacings such that the planets are beyond the 2:1 MMR.

We also present the first study of the actual shapes of the timescale distributions. In particular, in cases of broad or skewed distributions, knowing only the median (or mean) timescale can not provide a complete description of the distribution of timescales to instability. We find that the shapes of the distributions of the timescales are essentially the same for any K value away from a major MMR whereas near a major MMR the shape is very qualitatively different with a much slower decay above the median timescale (Figs. 30, 31). Both systems near and away from MMR show a similar exponential part in the stability timescale distribution. However, due to the MMR configuration, some of the systems enjoy increased stability manifested as a broader distribution to the higher time end. Note that the histograms of the timescale distributions are normalized such that $\sum_i n_i \Delta t_i = 1$, where Δt_i is the bin size in logarithm of time. The normalized number distribution for times lower than the median timescale (henceforth denoted as n_L) has an exponential shape; above the median timescale (henceforth denoted as n_R) the number distribution has a linear decay for all K away from major MMRs. The fitting formulae for n_L and n_R are given by

$$n_L = N_L \exp[(\log_{10} t - \log_{10} t_m(K))/t_L], \quad (\text{B5})$$

$$n_R = N_R - t_R \log_{10} t. \quad (\text{B6})$$

Here, N_L and N_R are the normalization constants for the peak amplitudes of the distributions, $t_m(K)$ is the median of the timescale distribution as a function of K , t_L and t_R are fitting constants characterizing the exponential index and the slope of the two curves, respectively. The best-fit values for N_L , N_R , t_L , and t_R are listed in Table 4. For a given K value, the median timescale can be estimated using Eq. B3 and then using the median timescale the shapes of the distributions can be obtained using Eqs. B5 and B6.

REFERENCES

- Adams, F. C. & Laughlin, G. 2003, *Icarus*, 163, 290
—, 2006a, *ApJ*, 649, 992
—, 2006b, *ApJ*, 649, 1004
Alexander, R. D., Clarke, C. J., & Pringle, J. E. 2006, *MNRAS*, 369, 229
Artymowicz, P. 1992, *PASP*, 104, 769
—, 1993, *ApJ*, 419, 166
Black, D. C. 1997, *ApJ*, 490, 171
Butler, R. P., Wright, J. T., Marcy, G. W., Fischer, D. A., Vogt, S. S., Tinney, C. G., Jones, H. R. A., Carter, B. D., Johnson, J. A., McCarthy, C., & Penny, A. J. 2006, *ApJ*, 646, 505
Chambers, J. E. 1999, *MNRAS*, 304, 793
Chambers, J. E., Wetherill, G. W., & Boss, A. P. 1996, *Icarus*, 119, 261
Clarke, C. J., Gendrin, A., & Sotomayor, M. 2001, *MNRAS*, 328, 485
Cumming, A., Butler, R. P., Marcy, G. W., Vogt, S. S., Wright, J. T., & Fischer, D. A. 2008, *arXiv:0803.3357*
Duncan, M. J., Levison, H. F., & Lee, M. H. 1998, *AJ*, 116, 2067
Faber, J. A., Rasio, F. A., & Willems, B. 2005, *Icarus*, 175, 248
Fabrycky, D. & Tremaine, S. 2007, *ApJ*, 669, 1298
Ford, E. B. & Chiang, E. I. 2007, *ApJ*, 661, 602
Ford, E. B., Havlickova, M., & Rasio, F. A. 2001, *Icarus*, 150, 303
Ford, E. B., Kozinsky, B., & Rasio, F. A. 2000, *ApJ*, 535, 385
Ford, E. B. & Rasio, F. A. 2006, *ApJ*, 638, L45
—, 2007, *arXiv:astro-ph/0703163*
Ford, E. B., Rasio, F. A., & Yu, K. 2003, in *ASP Conf. Ser.* 294: Scientific Frontiers in Research on Extrasolar Planets, ed. D. Deming & S. Seager, 181–188
Gladman, B. 1993, *Icarus*, 106, 247
Goldreich, P., Lithwick, Y., & Sari, R. 2004, *ApJ*, 614, 497
Goldreich, P. & Sari, R. 2003, *ApJ*, 585, 1024
Goldreich, P. & Tremaine, S. 1980, *ApJ*, 241, 425
Greenberg, R. 1974, *Icarus*, 23, 51
Heap, S. R., Lindler, D. J., Lanz, T. M., Cornett, R. H., Hubeny, I., Maran, S. P., & Woodgate, B. 2000, *ApJ*, 539, 435
Hollenbach, D., Johnstone, D., Lizano, S., & Shu, F. 1994, *ApJ*, 428, 654
Holman, M., Touma, J., & Tremaine, S. 1997, *Nature*, 386, 254
Hut, P. 1980, *A&A*, 92, 167
Ida, S. & Lin, D. N. C. 2004a, *ApJ*, 604, 388
—, 2004b, *ApJ*, 616, 567
Ivanov, P. B. & Papaloizou, J. C. B. 2004, *MNRAS*, 353, 1161
Juric, M. & Tremaine, S. 2007, *arXiv:astro-ph/0703160*
Kokubo, E. & Ida, S. 1998, *Icarus*, 131, 171
—, 2002, *ApJ*, 581, 666
Lafrenière, D., Doyon, R., Marois, C., Nadeau, D., Oppenheimer, B. R., Roche, P. F., Rigaut, F., Graham, J. R., Jayawardhana, R., Johnstone, D., Kalas, P. G., Macintosh, B., & Racine, R. 2007, *ApJ*, 670, 1367
Lee, M. H. 2004, *ApJ*, 611, 517
Lee, M. H. & Peale, S. J. 2002, *ApJ*, 567, 596
Levison, H. F. & Morbidelli, A. 2007, *Icarus*, 189, 196

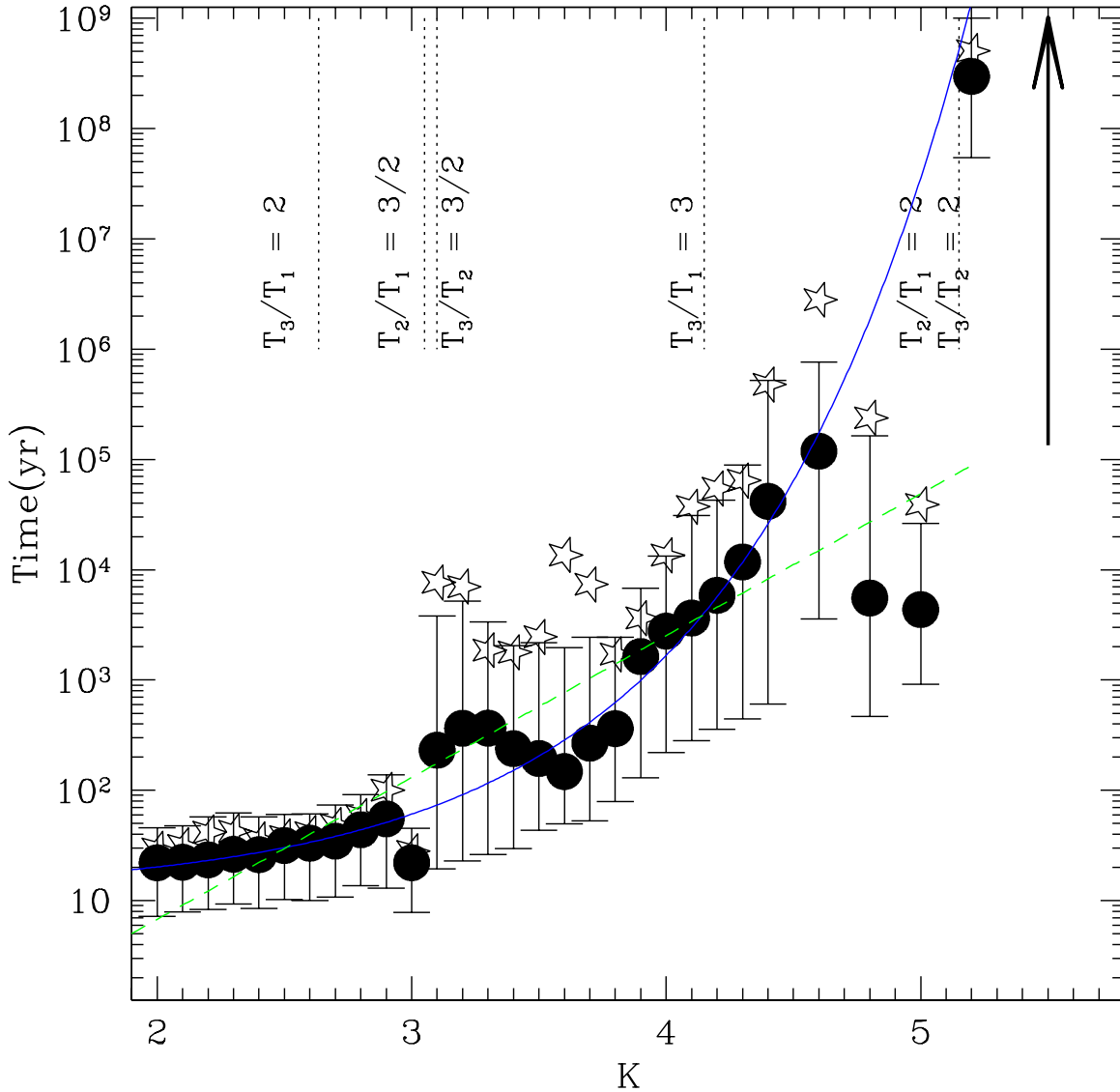


FIG. 29.— Instability growth timescale as a function of spacing parameter K . The filled circles are the medians of the distributions of stability timescales for the respective values of K . The bars show the $\pm 34\%$ range in the timescale. Note that they are not error bars, instead they represent the distribution of the stability timescales. The medians are shown in the plot because the distributions are skewed towards greater timescales. The open stars show the mean of the timescale distribution. Signatures of some major resonances can be noticed in the sudden dips in timescale. The arrow indicates that most systems with $K = 5.5$ are stable for at least 10^9 yr. The starting point of the arrow represents the shortest instability timescale among our simulations. The solid line (blue) and the dashed line (green) show the empirical best fit lines predicting the medians of the stability timescale distributions given the K values (Eqs. B3, B4).

Lin, D. N. C. & Ida, S. 1997, *ApJ*, 477, 781
 Lin, D. N. C. & Papaloizou, J. 1986, *ApJ*, 307, 395
 Lissauer, J. J. 1995, *Icarus*, 114, 217
 Marzari, F. & Weidenschilling, S. J. 2002, *Icarus*, 156, 570
 Matsumura, S., Thommes, E. W., Chatterjee, S., & Rasio, F. A. 2008, in preparation
 Mazeh, T., Krymowski, Y., & Rosenfeld, G. 1997, *ApJ*, 477, L103
 Moorhead, A. V. & Adams, F. C. 2005, *Icarus*, 178, 517
 —. 2008, *Icarus*, 193, 475
 Mouillet, D., Larwood, J. D., Papaloizou, J. C. B., & Lagrange, A. M. 1997, *MNRAS*, 292, 896
 Murray, C. D. & Dermott, S. F. 2000, *Solar System Dynamics* (Cambridge University Press, 2000.)
 Naef, D., Mayor, M., Beuzit, J.-L., Perrier, C., Queloz, D., Sivan, J.-P., & Udry, S. 2005, in *ESA Special Publication*, Vol. 560, ESA Special Publication, ed. F. Favata & et al., 833
 Nagasawa, M., Ida, S., & Bessho, T. 2008, arXiv:0801.1368

Narita, N., Enya, K., Sato, B., Ohta, Y., Winn, J. N., Suto, Y., Taruya, A., Turner, E. L., Aoki, W., Tamura, M., Yamada, T., & Yoshii, Y. 2007a, arXiv:astro-ph/0702707
 Narita, N., Sato, B., Ohshima, O., & Winn, J. N. 2007b, arXiv:0712.2569
 Ogilvie, G. I. & Lubow, S. H. 2003, *ApJ*, 587, 398
 Papaloizou, J. C. B. & Terquem, C. 2001, *MNRAS*, 325, 221
 Rasio, F. A. & Ford, E. B. 1996, *Science*, 274, 954
 Sándor, Z. & Kley, W. 2006, *A&A*, 451, L31
 Sándor, Z., Kley, W., & Klagivik, P. 2007, *A&A*, 472, 981
 Shakura, N. I. & Syunyaev, R. A. 1973, *A&A*, 24, 337
 Shu, F. H., Johnstone, D., & Hollenbach, D. 1993, *Icarus*, 106, 92
 Simon, M. & Prato, L. 1995, *ApJ*, 450, 824
 Smith, B. A. & Terrile, R. J. 1984, *Science*, 226, 1421
 Takeda, G. & Rasio, F. A. 2005, *ApJ*, 627, 1001
 Terquem, C. & Papaloizou, J. C. B. 2002, *MNRAS*, 332, L39
 Thommes, E. W. 2005, *ApJ*, 626, 1033
 Veras, D. & Armitage, P. J. 2004, *MNRAS*, 347, 613
 Ward, W. R. 1993, *Icarus*, 106, 274

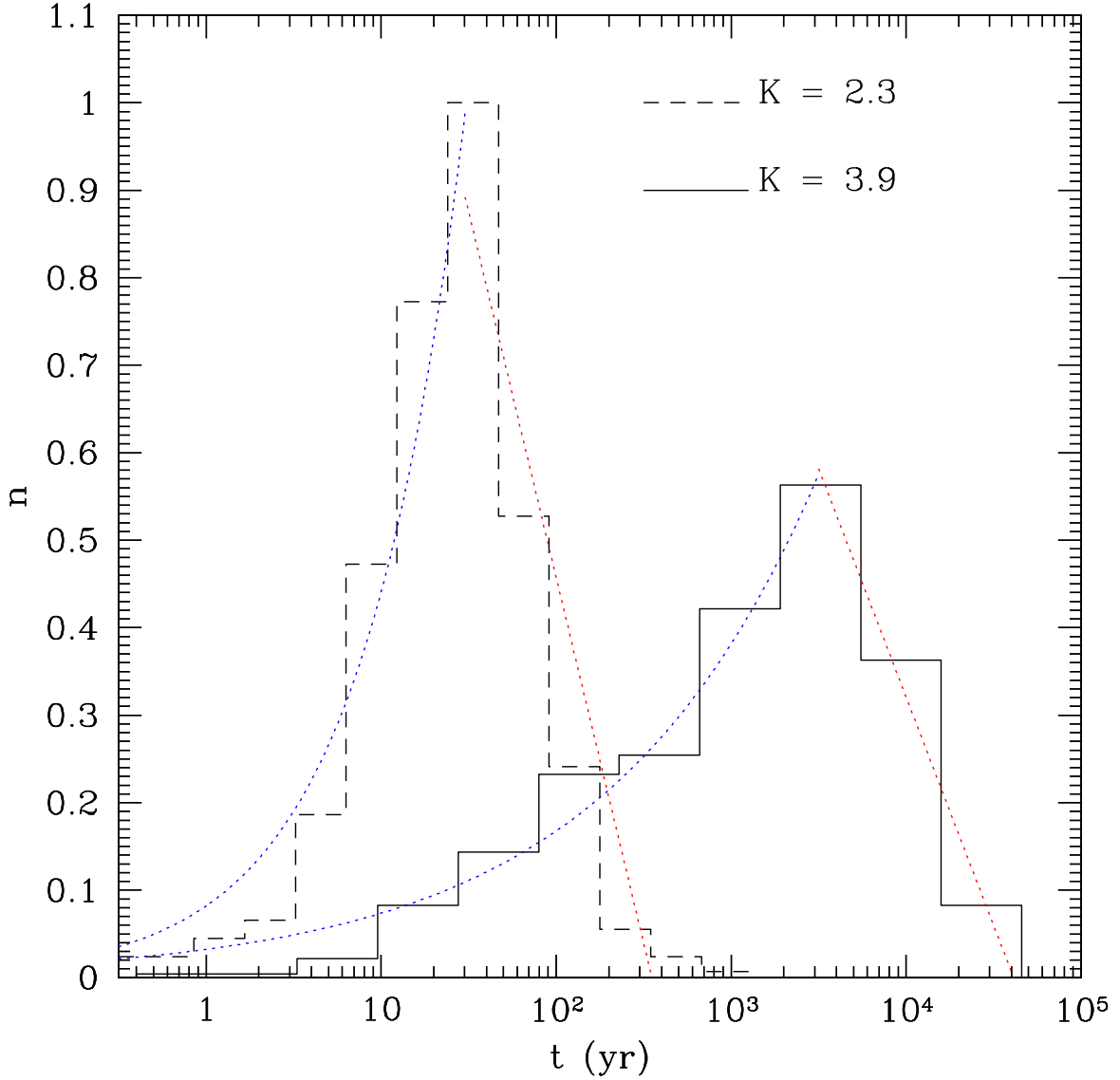


FIG. 30.— Histograms for the timescale distributions at two different K values both away from MMR. Note that times are shown in log scale. Each histogram shown here corresponds to 10^3 runs for that K value. The number distributions are normalized such that $\sum_i n_i \Delta t_i = 1$, where, Δt_i is the bin-size in logarithm of time. This normalization essentially makes the area under each histogram normalized to 1. The solid histogram corresponds to $K = 3.9$ and the dashed histogram corresponds to $K = 2.3$. Both these K values are away from any major MMR. The two histograms have essentially the same shape. The dotted (blue and red) curves show the analytical fitting curves for timescale distributions at the left and the right sides of the mode of the distributions. For systems with stability timescales less than the median of the distribution show an exponential shape, whereas, those with timescales higher than the median show a linear drop-off (see Eqs. B5, B6 and Table 4).

—. 1997, ApJ, 482, L211

Weidenschilling, S. J. & Marzari, F. 1996, Nature, 384, 619

Winn, J. N., Johnson, J. A., Marcy, G. W., Butler, R. P., Vogt, S. S., Henry, G. W., Roussanova, A., Holman, M. J., Enya, K., Narita, N., Suto, Y., & Turner, E. L. 2006, ApJ, 653, L69

Winn, J. N., Noyes, R. W., Holman, M. J., Charbonneau, D., Ohta, Y., Taruya, A., Suto, Y., Narita, N., Turner, E. L., Johnson, J. A., Marcy, G. W., Butler, R. P., & Vogt, S. S. 2005, ApJ, 631, 1215

Wolf, A. S., Laughlin, G., Henry, G. W., Fischer, D. A., Marcy, G., Butler, P., & Vogt, S. 2007, ApJ, 667, 549

Wright, J. T., Marcy, G. W., Fischer, D. A., Butler, R. P., Vogt, S. S., Tinney, C. G., Jones, H. R. A., Carter, B. D., Johnson, J. A., McCarthy, C., & Apps, K. 2007, ApJ, 657, 533

Wu, Y. & Murray, N. 2003, ApJ, 589, 605

Zakamska, N. L. & Tremaine, S. 2004, AJ, 128, 869

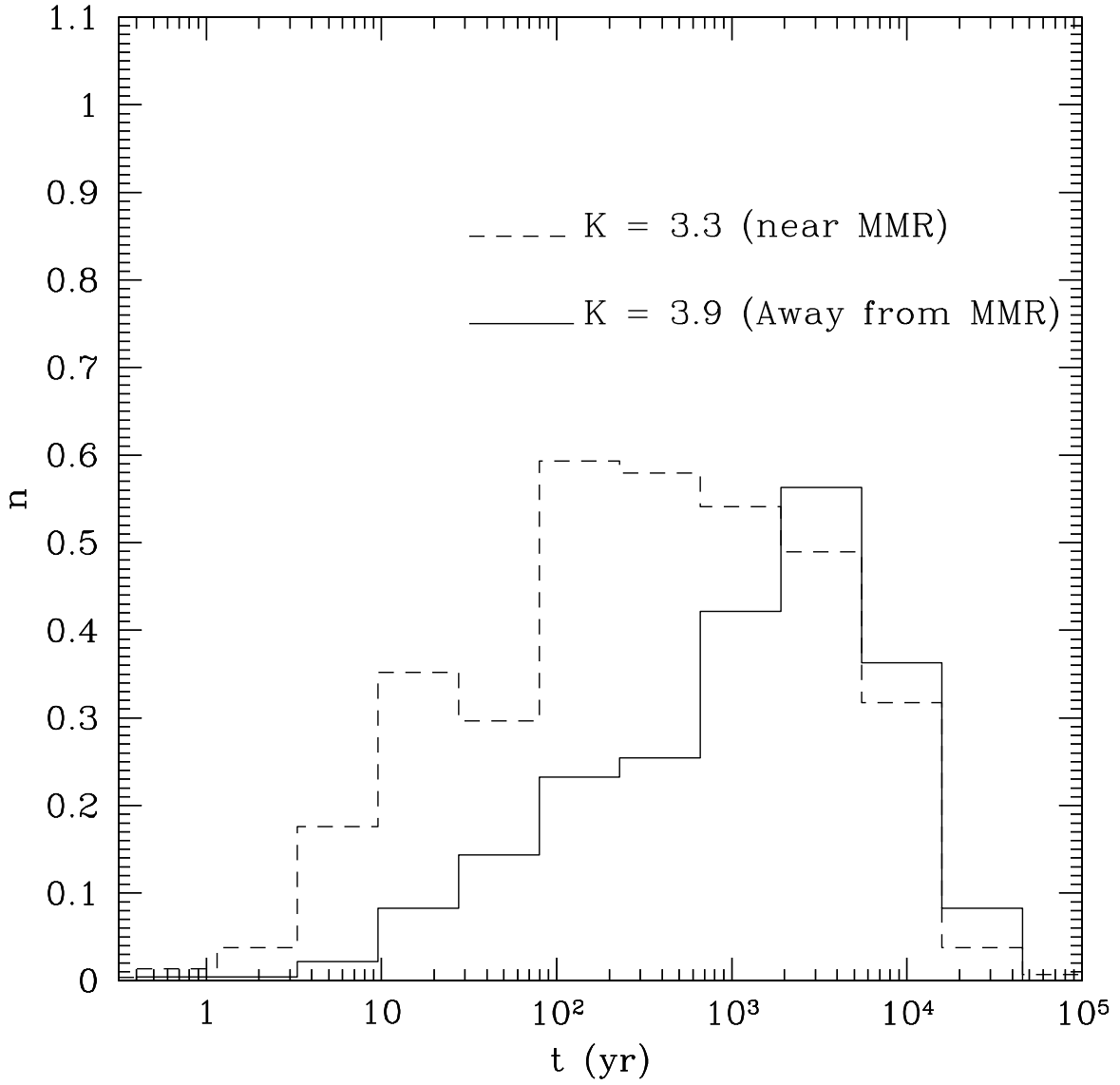


FIG. 31.— Histograms for the timescale distributions near and away from an MMR. Each histogram corresponds to 10^3 runs for that K value. We follow the same normalization scheme as mentioned earlier. $K = 3.3$ is near the K value for a $3 : 2$ commensurability between the periods of the first and the second as well as the second and the third planetary orbits (dashed line). $K = 3.9$ is away from MMR (solid line). The distributions near and away from MMR have somewhat similar shapes for times lower than the medians of the distributions. However, for times higher than the medians the decay is not as sharp near a MMR as for systems far from a MMR.

TABLE 4
FIT: TIMESCALE DISTRIBUTION
($n_{L,R}$)

K	t_L	N_L	t_R	N_R
2.0	0.719	0.714	1.728	3.716
2.1	0.669	0.775	1.138	2.649
2.2	0.582	0.886	0.778	1.971
2.3	0.595	0.864	0.836	2.129
2.4	0.663	0.867	1.193	2.816
2.5	0.530	0.996	1.559	3.628
2.6	0.482	1.153	1.286	3.065
2.7	0.589	1.004	1.112	2.806
2.8	0.582	1.002	1.167	3.01
2.9	0.713	0.800	0.584	1.791
3.0	0.624	1.715	1.412	3.141
3.1	0.810	0.512	0.095	0.522
3.2	2.343	0.206	0.082	0.484
3.3	1.447	0.283	0.203	0.968
3.4	1.051	0.462	0.188	0.889
3.5	0.533	1.238	0.180	0.869
3.6	0.395	3.700	0.201	0.929
3.7	0.811	0.937	0.143	0.753
3.8	0.744	1.085	0.245	1.140
3.9	1.211	0.415	0.522	2.409
4.0	1.488	0.353	0.349	1.811
4.1	1.399	0.379	0.160	0.975
4.3	1.684	0.346	0.204	1.292
4.4	2.650	0.218	0.127	0.953
4.8	1.066	4.910	0.102	0.710
5.0	0.767	73.831	0.209	1.242

^a Best fit values for the fitting parameters, N_L , t_L , N_R , and t_R predicting n_L , and n_R for a given K and the median of the stability timescale distribution $t_m(K)$.